Probability Distributions of Angle of Approach and Relative Velocity for Colliding Droplets in a Turbulent Flow

LIAN-PING WANG

Department of Mechanical Engineering, University of Delaware, Newark, Delaware, and Mesoscale and Microscale Meteorology Division, National Center for Atmospheric Research, Boulder, Colorado*

CHARMAINE N. FRANKLIN

Department of Atmospheric and Oceanic Sciences, McGill University, Montreal, Quebec, Canada

ORLANDO AYALA

Department of Mechanical Engineering, University of Delaware, Newark, Delaware

WOJCIECH W. GRABOWSKI

Mesoscale and Microscale Meteorology Division, National Center for Atmospheric Research, Boulder, Colorado

(Manuscript received 1 September 2004, in final form 26 June 2005)

ABSTRACT

Prediction of the effect of air turbulence on statistics relevant to a collision–coalescence process represents a key challenge in the modeling of cloud microphysics. In this paper, collision-related statistics for gravity-driven motion of droplets are considered and various probability distributions associated with geometric configuration and relative motion of colliding droplets are theoretically derived. The theoretical results agree well with numerical results obtained from direct numerical simulations (DNSs). In the absence of air turbulence, the probability distributions, calculated at the beginning of the time steps used for collision detection, nontrivially depend on the time step size. Next, a novel theory is developed to quantify the effect of turbulence on the angle-of-approach θ and radial relative velocity $|w_{r,c}|$ for colliding pairs. A logical decomposition is used to construct extended collision volumes for a specific level of radial motion caused by air turbulence. It is shown that the inward relative motion due to turbulent fluctuations dominates the effect of turbulence in modifying the probability distributions of θ and $|w_{r,c}|$. Two key dimensionless parameters are identified in the theory: one measures the effect of finite time step size in numerical collision detection and the second measures the relative magnitude of air turbulence. The theory is compared with 11 numerical experiments from DNS. It is shown that the theory captures the essential physics of the effect of air turbulence and provides a quantitatively good representation of the statistics for θ. For most numerical experiments, the theory predicts $\langle\theta\rangle$ to within 5%. The probability distribution of $|w_{r,c}|$ is more sensitive to the influence of air turbulence and shows larger intermittency at large $|w_{r,c}|$ than what is assumed in the theory. The theoretical framework developed here may be of value to other problems involving gravitational settling and weak turbulence, such as parameterization of collision kernel and hydrodynamic interactions of droplets in warm rain processes.

* The National Center for Atmospheric Research is sponsored by the National Science Foundation.

Corresponding author address: Dr. Lian-Ping Wang, Dept. of Mechanical Engineering, 126 Spencer Laboratory, University of Delaware, Newark, DE 19716-3140.
E-mail: lwang@udel.edu

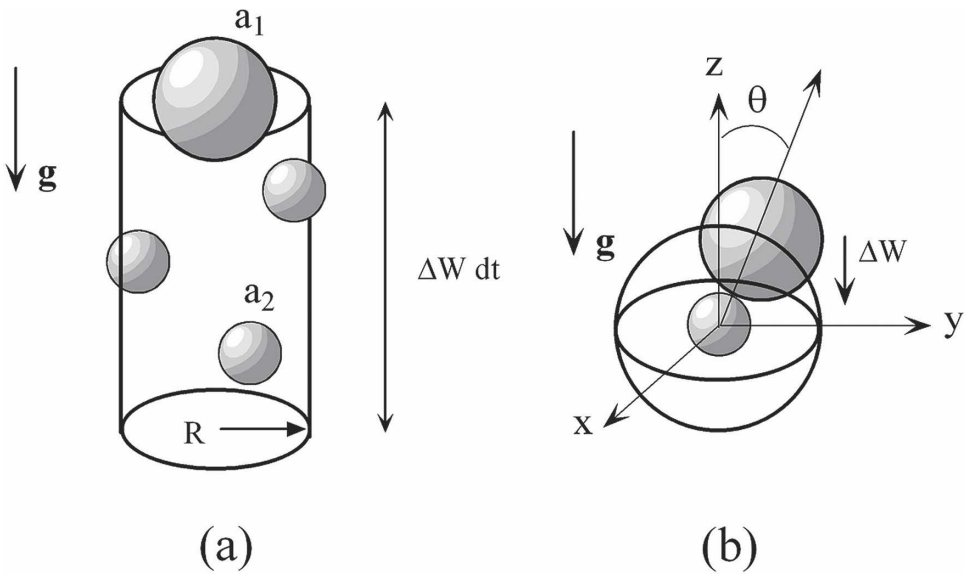

FIG. 1. Two kinematic formulations of geometric gravitational kernel. (a) The cylindrical formulation based on swept volume; and (b) the spherical formulation based on net volume influx.

1. Introduction

Collision-induced coalescences of particles and droplets in a turbulent fluid are of importance to a wide variety of applications in engineering and a host of phenomena in nature. Examples include motion of cloud droplets in the atmosphere (Pruppacher and Klett 1997), sedimentation in rivers (Tory 1996), transport of dust and pollutants in air (Seinfeld and Pandis 1997), and deposition of pulp fibers in paper manufacturing (Smook 1982). The motivation here is to understand and quantify the effect of turbulence on the collision rates of droplets in atmospheric warm clouds. Cloud droplets of radii larger than 10 to 15 μm grow primarily by collision coalescence, leading to the formation of warm rain (Pruppacher and Klett 1997). For this specific application, the collision–coalescence process is driven mainly by the gravitational effect but air turbulence has been shown to have a significant impact on the collision rate when either droplets are small or collisions between droplets of similar sizes are considered (Franklin et al. 2005; Wang et al. 2005a). It has been recognized that air turbulence broadens the distributions of relative velocity and angle of approach of colliding pairs (Arenberg 1939; Manton 1974; Reuter et al. 1988; Khain and Pinsky 1997; Franklin et al. 2005).

In a stagnant air, collision coalescences are caused by the difference in terminal velocities if the system contains droplets of different sizes. The average rate of collision per unit volume between droplets of two distinct radii a_1 and a_2 ($a_2 < a_1$) can be written as

$$\langle \dot{\mathcal{N}}_{12} \rangle = \pi R^2 (W_1 - W_2) E_{12} n_1 n_2, \tag{1}$$

where $R \equiv a_1 + a_2$ is the geometric collision radius, W_1 and W_2 denote the terminal velocities for the two sizes, n_1 and n_2 are the average number concentrations, and E_{12} is the collision efficiency measuring the effect of local hydrodynamic interactions. The above expression implies a geometric collision kernel Γ of $\pi R^2 (W_1 - W_2)$ or the geometric capture volume swept by a droplet of radius a_1 due to the differential settling velocity $\Delta W \equiv W_1 - W_2$, as shown in Fig. 1a. Such a geometric–kinematic description is known as the cylindrical formulation and is applicable to simple gravitational collision coalescence without background air turbulence, but becomes inaccurate for turbulent collision (Wang et al. 1998b, 2005c).

The more general approach to geometric collision is the spherical formulation originally developed by Saffman and Turner (1956), which states

$$\Gamma = 2\pi R^2 \langle |w_r(r = R)| \rangle, \tag{2}$$

where the radial relative velocity is defined in terms of the center-to-center separation vector $\mathbf{r}$ (pointing from a droplet of radius a_2 to a droplet of radius a_1), the velocity $\mathbf{V}_1$ of the a_1 droplet, and the velocity $\mathbf{V}_2$ of the a_2 droplet as $w_r = \mathbf{r} \cdot (\mathbf{V}_1 - \mathbf{V}_2)/r$ with $r = |\mathbf{r}|$. The angle brackets denote averages over all orientations of $\mathbf{r}$ and the spatial locations of the a_2 droplets. In the spherical formulation, the geometric collision kernel is viewed as the rate of volume influx through the geometric collision spherical surface of radius R (Fig. 1b). In Eq. (2), the area ($2\pi R^2$) represents the area of the spherical collision surface where the relative motion is toward each other ($w_r < 0$).

Within this spherical formulation, $w_r(r = R)$ depends on the polar angle θ measured with respect to the vertical direction (Fig. 1b), namely, for the gravitational collision,

$$w_r(r = R) = -\Delta W \cos\theta. \tag{3}$$

Therefore, w_r is negative for exactly half of the surface defined by $0 \le \theta \le \pi/2$. The rate of volume influx through the same portion of the surface can be calculated as

$$\int_0^{\pi/2} 2\pi(R\sin\theta)R\,d\theta\,|w_r| = 2\pi R^2\Delta W \int_0^{\pi/2} \sin\theta\cos\theta\,d\theta$$

$$= \pi R^2\Delta W, \tag{4}$$

giving the expected geometric collision kernel and

$$\langle|w_r(r = R)|\rangle^{(g)} = \Delta W/2, \tag{5}$$

where the superscript (g) denotes contribution due to the gravitational collision mechanism only (hereafter referred to as the base case). Therefore, $|w_r|$ for any droplet pair separated by a distance R varies from 0 to ΔW with a mean of $\Delta W/2$.

It has long been recognized that air turbulence can increase the geometric capture volume or the relative velocity such that $\langle|w_r(r = R)|\rangle$ are usually larger than $\langle|w_r(r = R)|\rangle^{(g)}$ leading to a geometric collision kernel larger than that of the base case (Arenberg 1939; Saffman and Turner 1956; Manton 1974; Reuter et al. 1988; Khain and Pinsky 1997; Franklin et al. 2005; Wang et al. 2005a).

The above formulations assume that droplets are uniformly distributed in space. When droplets have finite relative inertia, namely, the inertial response time of the droplets $\tau_p = 2\rho_p a^2/(9\mu)$ is comparable to the Kolmogorov time scale, τ_k, of the air turbulence, droplets are known to accumulate in regions of high strain and low vorticity (Maxey 1987). This preferential concentration effect can significantly increase the average collision kernel since the local collision rate is proportional to the second-order moment of local concentrations. Here ρ_p is the density of a droplet, μ is the fluid dynamic viscosity. The spherical formulation has been extended to include the preferential concentration effect by Sundaram and Collins (1997) and Wang et al. (1998b, 2000) and becomes

$$\Gamma = 2\pi R^2\,\langle|w_r(r = R)|\rangle g_{12}(r = R). \tag{6}$$

The additional factor g_{12} is the radial distribution function and measures the effect of preferential concentration on the pair number density at separation $r = R$. In direct numerical simulations (DNS), g_{12} can be computed, at any given time, as

$$g_{12}(r) = \frac{N_{\text{pair}}/V_s}{N_1N_2/V_B}, \tag{7}$$

where N_{pair} is the total number of pairs detected with separation distance falling within a thin spherical shell of average radius r, V_s is the volume of the spherical shell, N_1 is the total number of a_1 droplets used in the simulation, and N_2 is the total number of a_2 droplets. Also, V_B is the volume of the computational domain. The interpretation of $\langle|w_r(r = R)|\rangle$ remains the same. In the presence of gravity, the kinematic properties are no longer spherically symmetric, but the above formulation should still apply since the kinematic properties are understood as being averaged over all orientations (Wang et al. 1998b, 2005c). In this paper, we consider statistics related to the relative velocity only; the effect of particle clustering can be treated separately through g_{12} but will not be discussed any further in this paper.

It is important to point out that the relative velocities and the radial distribution function that appeared in the above formulations are kinematic properties of the particle pairs, namely, they are calculated, using field data at a single time instant, by making use of all pairs at a given separation. Of course, averaging over a multiple of uncorrelated time instants can be taken to reduce statistical uncertainties. We also use the term kinematic at-contact pairs to represent all kinematic pairs having a center-to-center separation equal to R. On the other hand, dynamically colliding pairs refer to the subset of particle pairs that actually collide; the term dynamic implies that the distance between a pair must be followed over time in order to determine whether the pair will collide. In this paper, we will focus mainly on dynamic pair statistics. We will demonstrate that the dynamic pair statistics are very different from the kinematic pair statistics, as noted previously by Mei and Hu (1999) and Wang et al. (2000, 2005c) for the mean relative velocity.

In an attempt to understand how turbulence modifies the relative motion of colliding pairs relative to the base case driven only by gravity, Franklin et al. (2005) investigated the probability distributions of $|w_r|$ and geometric configuration for colliding pairs. At any instant, the relative position configuration of a colliding pair can be represented by the polar angle θ (see Fig. 1b) as the relative motion is statistically independent of the azimuthal angle even in turbulent airflow. The distribution of θ for colliding droplets in a turbulent flow was previously discussed qualitatively in Pinsky et al. (2000). Following Pinsky et al. (2000), Franklin et al. (2005) termed θ the angle of approach and studied numerically the probability distribution of θ at several different levels of airflow dissipation rate ε. They found

that both the mean and variance of θ increase with ε. While θ can only vary from 0° to 90° for the base case, they showed that θ could take any value from 0° to 180° so that an a_1 droplet may approach an a_2 droplet from below because of turbulent fluid motion. Their DNS data also indicated that the mean and variance of $|w_{r,c}|$, that is, $|w_r|$ based on numerically detected colliding pairs, vary with ε. These probability distributions and average statistics provide insightful details of the effect of air turbulence on the geometric collision process.

In this paper, we will provide a rigorous and thorough theoretical treatment of these statistics. In section 2, we first consider the base case of gravitational collisions without air turbulence for two purposes: 1) to illustrate the notion of geometric interpretations using this simple setting and 2) to reveal the influence of the time step size used in the collision detection in terms of a dimensionless parameter $\tilde{\delta} \equiv \Delta W\, dt/R$.[1] We then extend the theory in section 3 to include the effect of turbulent motion, which will express the probability distributions in terms of $\tilde{\delta}$ and a second dimensionless parameter closely related to the dimensionless kinematic radial relative velocity. These theoretical predictions will be compared to results from DNS in section 4. Finally conclusions are summarized in section 5. Although in this paper the discussion is limited to statistics for geometrically colliding pairs, it is believed that the theoretical understanding developed here is relevant to the previously observed enhancement of collision efficiency by air turbulence (de Almeida 1979; Koziol and Leighton 1996; Pinsky et al. 1999; Wang et al. 2005b).

2. Theory for the base case without air turbulence

a. Infinitesimal time step

We shall first consider gravitational collision without air turbulence. We have seen in the introduction that, even for this base case, $|w_r|$ varies with θ and takes a value ranging from 0 to ΔW. It is instructive to inquire about the probability distribution of $|w_r|$, which, by definition, satisfies

$$\int_0^{\Delta W} p(|w_r|)\, d|w_r| = 1.0, \tag{8}$$

$$\int_0^{\Delta W} |w_r| p(|w_r|)\, d|w_r| = \langle |w_r| \rangle = \Delta W/2. \tag{9}$$

[1] Throughout this paper, a tilde (˜) over a quantity implies that the quantity is normalized by the collision radius R if the quantity has the dimension of length, or by the average kinematic radial relative velocity $\Delta W/2$ of the base case if the quantity has the dimension of velocity.

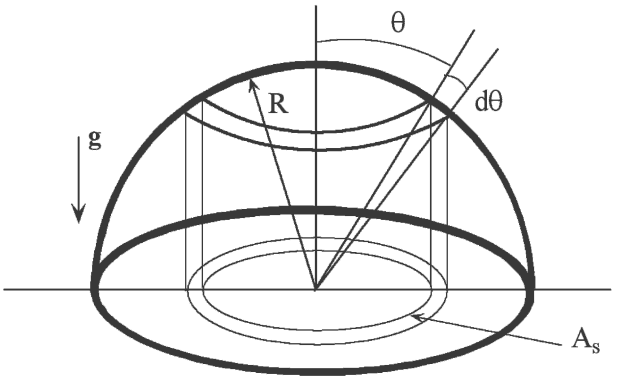

FIG. 2. An alternative interpretation of $p(\theta)$ for the gravitational case.

Using Eq. (4) and Eq. (9), we can show that the probability distribution of the kinematic at-contact relative velocity is

$$p(|w_r|) = \begin{cases} 1/\Delta W, & \text{if} \quad 0 \le |w_r| \le \Delta W; \\ 0, & \text{otherwise.} \end{cases} \tag{10}$$

This result is also consistent with Eq. (8). Therefore, the probability distribution of $|w_r|$ is uniform over the range of $|w_r|$ from 0 to ΔW.

In terms of the normalized variable $\tilde{w}_r \equiv |w_r|/\langle |w_r| \rangle^{(g)} = |w_r|/(0.5\Delta W)$, we have

$$p(\tilde{w}_r) = \begin{cases} 0.5, & \text{if} \quad 0 \le \tilde{w}_r \le 2; \\ 0, & \text{otherwise,} \end{cases} \tag{11}$$

with a mean and standard deviation for $\tilde{w}_r$ of 1.0 and 0.5774, respectively.

Next we derive the probability distribution of θ based on pairs that actually collide in an infinitesimal time interval dt. This is equal to the ratio of the volume influx over a differential surface defined by $d\theta$ to the total volume influx:

$$p(\theta)\, d\theta = \frac{(2\pi R \sin\theta)(R\, d\theta)|w_r|\, dt}{\pi R^2 \Delta W\, dt} = \sin(2\theta)\, d\theta; \tag{12}$$

namely,

$$p(\theta) = \begin{cases} \sin(2\theta), & \text{if} \quad 0 \le \theta \le \pi/2; \\ 0, & \text{otherwise.} \end{cases} \tag{13}$$

An alternative derivation of the same result with a better physical intuition is to take a plane perpendicular to the vertical axis and recognize that the flux is uniform over a circle of radius R (so again the total flux is $\pi R^2 \Delta W$). To convert to the polar angle representation, one may ask what is the projected area of a differential spherical surface onto the plane surface (Fig. 2). Since the projected area is $A_s = \pi R^2[\sin^2(\theta + d\theta) - \sin^2(\theta)] \approx 2\pi R^2 \sin\theta \cos\theta\, d\theta$, and $p(\theta)d\theta = A_s/\pi R^2$, we again obtain $p(\theta) = \sin(2\theta)$ for $0 \ge \theta \ge \pi/2$.

It follows that the mean and standard deviation for the angle of approach in the limit of $dt \to 0$ are

$$\langle\theta\rangle = \int_0^{\pi/2} \theta \sin(2\theta)\, d\theta = \frac{\pi}{4} \text{ rad} \quad \text{or} \quad 45° \tag{14}$$

$$\sqrt{\langle(\theta - \langle\theta\rangle)^2\rangle} = \left[\int_0^{\pi/2} \theta^2 \sin(2\theta)\, d\theta - \left(\frac{\pi}{4}\right)^2\right]^{1/2} = 0.341834 \text{ rad} \quad \text{or } 19.59°. \tag{15}$$

Next we focus our attention on just these pairs that collide dynamically within the infinitesimal time dt. These are a total of $\pi R^2 \Delta W\, dt\, n_1 n_2$ pairs per unit volume. We shall inquire about the probability density of finding $|w_{r,c}|$ at a particular value. Since $|w_{r,c}| = \Delta W \cos\theta$ and $d|w_{r,c}| = -\Delta W \sin\theta\, d\theta$, we have

$$\int_0^{\pi/2} p(\theta)\, d\theta = \int_0^{\Delta W} \sin(2\theta) \frac{d|w_{r,c}|}{\Delta W \sin\theta} = \int_0^{\Delta W} \frac{2}{\Delta W} \frac{|w_{r,c}|}{\Delta W}\, d|w_{r,c}|; \tag{16}$$

therefore,

$$p(|w_{r,c}|) = \begin{cases} 2|w_{r,c}|/(\Delta W)^2, & \text{if} \quad 0 \le |w_{r,c}| \le \Delta W; \\ 0, & \text{otherwise.} \end{cases} \tag{17}$$

In terms of the normalized variable $|\tilde{w}_{r,c}| \equiv |w_{r,c}|/(0.5\Delta W)$ we have

$$p(|\tilde{w}_{r,c}|) = \begin{cases} 0.5|\tilde{w}_{r,c}|, & \text{if} \quad 0 \le |\tilde{w}_{r,c}| \le 2; \\ 0, & \text{otherwise.} \end{cases} \tag{18}$$

The mean and standard deviation for $|\tilde{w}_{r,c}|$ are

$$\langle|\tilde{w}_{r,c}|\rangle = 4/3, \quad \sigma_{|\tilde{w}_{r,c}|} = \sqrt{\langle|\tilde{w}_{r,c}|^2\rangle - (\langle|\tilde{w}_{r,c}|\rangle)^2} = \sqrt{2}/3 = 0.4714. \tag{19}$$

Therefore, we obtain

$$\langle|\tilde{w}_{r,c}|\rangle = \frac{4}{3}\langle\tilde{w}_r\rangle, \tag{20}$$

namely, the mean relative velocity based on dynamic colliding pairs is 33% larger than the mean relative velocity based on kinematic at-contact pairs.

b. Finite time step

In direct numerical simulations (Sundaram and Collins 1997; Wang et al. 2000, 2005b; Franklin et al. 2005), the trajectories of droplets are followed by solving their equations of motion. Collision events are detected dynamically by examining the separation distance of all nearby pairs. A collision is registered if the distance r changes from $r > R$ to $r < R$. In actual code implementation, a finite time step size dt must be used and the details of the collision event detection may differ from one implementation to another.

Consider any time step from time $t^{(n)}$ to $t^{(n+1)} = t^{(n)} + dt$. In the study of Franklin et al. (2005) developed at McGill University (MU), the separation distance $r(t)$ for $t^{(n)} \le t < t^{(n+1)}$ was represented by a linear interpolation using the information at $t = t^{(n)}$ only (i.e., using $r[t^{(n)}]$ and $w_r\{r = r[t^{(n)}]\}$). While in the studies conducted at the University of Delaware (UD; Wang et al. 1998a, 2000; Zhou et al. 2001; Wang et al. 2005b), the velocities and positions at $t = t^{(n+1)}$ were obtained first, and a third-order polynomial representation was used to describe $r(t)$ during the time step interval using the information of r and w_r at both $t = t^{(n)}$ to $t = t^{(n+1)}$. The UD implementation allows for three possible types of collision events (Wang et al. 1998a) due to the nonlinear representation of $r(t)$: namely, (i) type I collisions with $r[t^{(n)}] > R$ and $r[t^{(n+1)}] < R$; (ii) type II collisions with $r[t^{(n)}] > R$ and $r[t^{(n+1)}] > R$ but $r(t) < R$ during part of the time interval; (iii) type III collisions with $r[t^{(n)}] < R$ and $r[t^{(n+1)}] < R$ but $r(t) > R$ during part of the time interval. For the base case without air turbulence, the two implementations are identical. For the general case of turbulent collision, the UD implementation is more accurate for large time steps. When the time step size is properly controlled such that type I collisions dominate, and types II and III collisions are very unlikely to occur, the two implementations should yield the same result for collision counts.

In both implementations, when a pair were found to collide during the time interval $t^{(n)} \le t < t^{(n+1)}$, the positions and velocities of the pair at the beginning of the time step $[t = t^{(n)}]$ were saved in order to later process the probability distributions for θ and $|w_r|_c$. As will be shown below, it is very important to distinguish the information saved at $t = t^{(n)}$ from the information at the instant of the collision when $r(t) = R$.

For the base case, two droplets separated at a center-to-center distance of as much as $R + \Delta W\, dt$ may collide during the time interval. Therefore, if $\delta \equiv \Delta W\, dt$ is comparable to R, the probability distributions of θ and $|w_{r,c}|$ obtained with information at $t = t^{(n)}$ will differ from the theoretical results obtained in section 2a.

In principle, the actual geometric configuration and relative velocity at the instant of collision contact can be interpolated or extrapolated in DNS to remove the effect of time step size. However, we shall extend our theory for infinitesimal time step, presented in the last section, to finite time step size for several reasons. First, the implementation of highly accurate interpolations or extrapolations of the relative motion for all colliding pairs in a system consisting of 100 000 droplets can be tedious and time consuming. Second, previous theoretical formulations such as Reuter et al. (1988); Sundaram and Collins (1997) often considered finite-

time delays in their derivations, for the reason that a collision event is a dynamic process in which the interparticle separation $r(t)$ is dynamically changed from $r(t) > R$ to $r(t) \le R(t)$. Third, efforts have begun to be made to experimentally measure collision-related statistics such as relative velocities and local pair clustering (Meng et al. 2004; Yang et al. 2005); in these experiments, only positions of particles at discrete times are available. Finally, in computing kinematic relative velocities and pair concentrations, pairs at a range of finite separations, instead of only at contact pairs, are routinely used to increase the available number of samples such that statistical uncertainties can be better controlled (Wang et al. 2000; Zhou et al. 2001). For these various reasons, pair statistics during a finite time or within a finite separation right before the actual collisions are central to the understanding and quantification of collision interactions. Therefore, studying the statistics at finite time steps are broadly motivated, in particular we expect that the theoretical results developed here can help others better interpret experimental observations, in addition to clarifying our own DNS results. Having theories for both infinitesimal time steps and finite time steps allows us to separate out the time step effect from other physical effects. Alternatively, by understanding the time step effect, we can offer more flexibility to DNS and experimental observations.

We shall now show that these probability distributions based on the simulation data can be rigorously derived for the base case. Since the relative motion is constant and is pointing in the vertical direction, the volume that contributes to the influx or geometric collision, as illustrated in Fig. 3, is a region bounded at the bottom by the original half geometric collision spherical surface of $\theta \le \pi/2$, and at the top by a half-spherical surface created by simply shifting the original spherical surface vertically upward by δ, and on the sides by a cylindrical surface of height δ and radius R. This volumetric region will be referred to as the collision volume. If the center of any a_1 droplet is located in this volume, this droplet will collide with an a_2 droplet during $t^{(n)} \le t < t^{(n+1)}$. It is important to note that the total volume of this bounded region is $\pi R^2\delta$, therefore, the net rate of geometric collisions, which is proportional to $\pi R^2\delta/dt$ or $\pi R^2\Delta W$, does not depend on the time step size and all the kinematic formulations discussed in the introduction remain valid when compared to DNS results (Wang et al. 2000; Zhou et al. 2001).

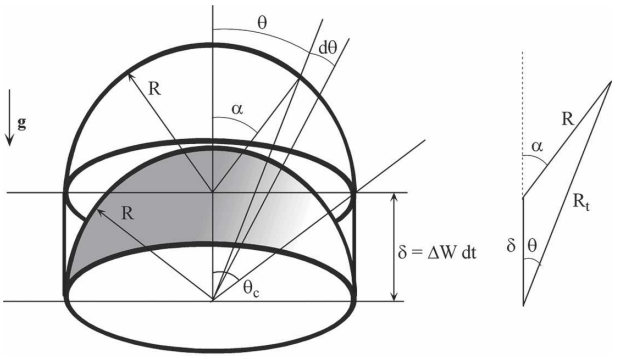

FIG. 3. The volume entering the geometric collision spherical surface during a finite time interval dt as used in direct numerical simulations.

Assuming dynamic colliding droplets are distributed uniformly in this bounded region, the probability for the angle of approach, $p(\theta)$, is then the differential overlap volume of the conical shell of polar angle from θ to $\theta + d\theta$ and the above bounded region, divided by the total volume $\pi R^2\delta$. For $\theta \le \theta_c \equiv \arctan(R/\delta)$, we then have

$$p(\theta)\,d\theta = \frac{2\pi \int_{r=R}^{r=R_t} r^2\,dr\sin\theta\,d\theta}{\pi R^2\delta} = \frac{2\sin\theta(R_t^3 - R^3)}{3R^2\delta}\,d\theta, \tag{21}$$

where R_t is the radial distance of the top surface of the bounded volume at polar angle θ. With the help of the triangle graph on the right in Fig. 3, R_t can be related to R, δ, and θ as

$$R_t = \delta\cos\theta + \sqrt{R^2 - \delta^2\sin^2\theta}, \tag{22}$$

while for $\theta > \theta_c$,

$$p(\theta)d\theta = \frac{2\pi \int_{r=R}^{r=R/\sin\theta} r^2\,dr\sin\theta\,d\theta}{\pi R^2\delta},$$

$$= \frac{2}{3}\frac{R}{\delta}\left(\frac{1}{\sin^2\theta} - \sin\theta\right)d\theta. \tag{23}$$

Putting this altogether and introducing $\tilde{\delta} = \delta/R = \Delta W\,dt/R$, we obtain the probability distribution of θ as

$$p(\theta;\tilde{\delta}) = \begin{cases} 2\sin\theta\left[\left(\tilde{\delta}\cos\theta + \sqrt{1 - \tilde{\delta}^2\sin^2\theta}\right)^3 - 1\right]/(3\tilde{\delta}), & \text{if} \quad \theta \le \arctan 1/\tilde{\delta}; \\ 2[(\sin\theta)^{-2} - \sin\theta]/(3\tilde{\delta}), & \text{if} \quad \arctan(1/\tilde{\delta}) < \theta < \pi/2; \\ 0, & \text{otherwise.} \end{cases} \tag{24}$$

It can be shown that the above probability distribution reduces to Eq. (13) as $\tilde{\delta} \to 0$. For finite dt or $\tilde{\delta}$, however, the probability distribution of θ depends on $\tilde{\delta}$.

By the similar reasoning as used in deriving Eq. (16), we can relate the probability distribution of $|w_{r,c}|$ to $p(\theta;\tilde{\delta})$,

$$p(|w_{r,c}|; \tilde{\delta}) = \frac{p(\theta; \tilde{\delta})}{\Delta W \sin\theta}. \tag{25}$$

Therefore, we obtain the following result:

$$p(|\tilde{w}_{r,c}|; \tilde{\delta}) = \begin{cases} [(1 - 0.25|\tilde{w}_{r,c}|^2)^{-1.5} - 1]/(3\tilde{\delta}), & \text{if } |\tilde{w}_{r,c}| \le 2\tilde{\delta}\Big/\sqrt{1+\tilde{\delta}^2}; \\ \left\{\left[0.5\tilde{\delta}|\tilde{w}_{r,c}| + \sqrt{1 - \tilde{\delta}^2(1 - 0.25|\tilde{w}_{r,c}|^2)}\right]^3 - 1\right\}/(3\tilde{\delta}), & \text{if } 2\tilde{\delta}\Big/\sqrt{1+\tilde{\delta}^2} \le |\tilde{w}_{r,c}| \le 2.0; \\ 0, & \text{otherwise.} \end{cases} \tag{26}$$

This general result can recover Eq. (18) if we let $\tilde{\delta} \to 0$ or $dt \to 0$. Note that the two nonzero regions in Eq. (24) are interchanged when converted to Eq. (26).

3. Theory for turbulent collision

The theory and geometric interpretation developed in the previous section for the base case shall now be extended to include the effect of turbulent air motion or the turbulent collision case. The collision volume shown in Fig. 3 needs to be properly expanded to account for the added relative motion due to turbulent air motion.

a. Decomposition of radial relative motion

The strategy is to include turbulence effects in two steps. First, it is assumed that the air turbulence alone introduces a radial relative motion q_r. In the first step, q_r is assumed to be a constant and spherically symmetric. In the second step, the result from the first step is integrated with the probability distribution of q_r. This two-step procedure makes it possible to formulate a theory for the probability distribution of the angle of approach using geometric interpretations. Furthermore, as will be shown later, it facilitates the conversion of this probability distribution to the probability distribution of radial relative velocity for colliding pairs.

The total instantaneous relative velocity is

$$w_r = -(\Delta W \cos\theta + q_r), \tag{27}$$

where q_r is positive if turbulence induces inward relative motion. It is further assumed that q_r has a Gaussian probability distribution of zero mean and standard deviation σ_q, namely,

$$p(q_r) = \frac{1}{\sqrt{2\pi}\sigma_q} \exp\left(-\frac{q_r^2}{2\sigma_q^2}\right). \tag{28}$$

The true probability distribution of q_r is likely to be non-Gaussian. It has been shown by Sundaram and Collins (1997) and Wang et al. (2000) using DNS that the probability distributions of particle relative velocity are better fitted by stretched exponential. Another good alternative is the lognormal distribution (e.g., Falkovich et al. 2002). Here we chose Gaussian distribution to simplify the derivation.

The polar angle θ may also be viewed as a random variable. If the a_1 droplets are assumed to be found with uniform probability on the surface of the collision sphere, the probability distribution of the polar angle for kinematic at-contact droplet pairs is the percentage of collision-sphere surface covered by differential polar angle $d\theta$, divided by $d\theta$, and is

$$p_0(\theta) = \left[\frac{(2\pi R \sin\theta) R\, d\theta}{4\pi R^2}\right]\frac{1}{d\theta} = 0.5 \sin\theta. \tag{29}$$

The average total radial velocity can then be calculated as

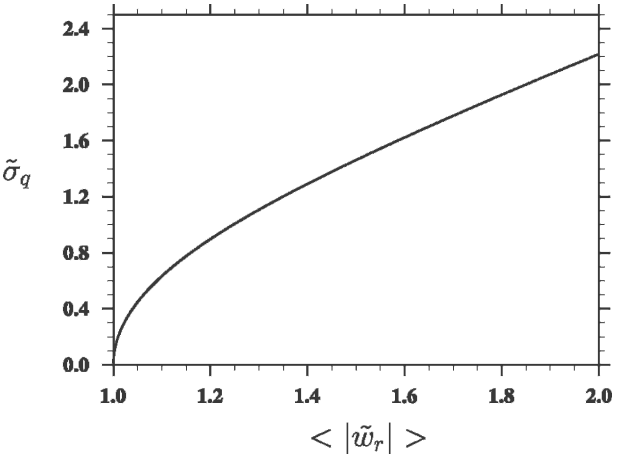

FIG. 4. The relationship between $\tilde{\sigma}_q$ and $\langle|\tilde{w}_r|\rangle$ according to Eq. (30).

TABLE 1. The parameter setting, $\langle|\tilde{w}_r|\rangle$, and $\tilde{\sigma}_q$ for DNS runs conducted at MU ($a_1 = 20\ \mu$m, $a_2 = 10\ \mu$m, $\Delta W = 3.6958$ cm s^{-1}).

Run ID	Run1	Run2	Run3	Run4	Run5
N	—	80	120	180	240
ε (cm^2 s^{-3})	0	95	280	656	1535
dt (μs)	100	800	200	80	50
$\tilde{\delta}$	0.123	0.985	0.246	0.0985	0.0616
No. of pairs	2564	7980	3284	2315	2737
R_λ	—	33	40	48	55
$\tilde{w}_r$, DNS	1.0	1.0093	1.074	1.150	1.489
$\tilde{\sigma}_q$, Eq. (30)	0.0	0.192	0.544	0.775	1.443

$$\langle|w_r|\rangle = \int_0^\pi p_0(\theta)\, d\theta \int_{-\infty}^{\infty} p(q_r)|w_r|\, dq_r$$
$$= \int_0^\pi 0.5 \sin\theta\, d\theta \frac{1}{\sqrt{2\pi}\sigma_q} \exp\left(-\frac{q_r^2}{2\sigma_q^2}\right) dq_r |\Delta W \cos\theta + q_r|$$
$$= \frac{\sigma_q}{\sqrt{2\pi}} \exp\left[-\frac{(\Delta W)^2}{2\sigma_q^2}\right] + \frac{(\Delta W)^2 + \sigma_q^2}{2\Delta W} \mathrm{erf}\left(\frac{\Delta W}{\sqrt{2}\sigma_q}\right), \quad (30)$$

where the standard error function is defined as $\mathrm{erf}(x) = (2/\sqrt{\pi}) \int_0^x e^{-y^2}\, dy$. In the limit of $\Delta W \to 0$, the above result reduces to $\langle|w_r|\rangle = \sigma_q\sqrt{2/\pi}$, as expected for turbulent relative motion without gravity (Wang et al. 1998b). On the other hand, if the turbulence effect is very weak compared to gravity or $\sigma_q \to 0$, we recover the expected result of $\langle|w_r|\rangle = 0.5\Delta W$. Equation (30) implies a one-to-one relationship between the two nondimensional variables $\langle|\tilde{w}_r|\rangle \equiv \langle|w_r|\rangle/(0.5\Delta W)$ and $\tilde{\sigma}_q \equiv \sigma_q/(0.5\Delta W)$, which is shown in Fig. 4. We observe that $\tilde{\sigma}_q$ increases quickly with $\langle|\tilde{w}_r|\rangle$ when the air turbulence is weak or $\tilde{\sigma}_q$ is small. Also, $\tilde{\sigma}_q$ can be larger than $\langle|\tilde{w}_r|\rangle$ since a very strong turbulence will result in $\tilde{\sigma}_q = \sqrt{\pi/2}\,\langle|\tilde{w}_r|\rangle = 1.2533\langle|\tilde{w}_r|\rangle$ because most of $|w_r|$ are less than σ_q in the Gaussian distribution.

To validate the theoretical predictions in this paper, we shall introduce five sets of DNS data generated at MU and six sets of DNS data independently generated at UD. The relevant parameters including grid resolution N in each direction, average flow dissipation rate ε, and the normalized time step $\tilde{\delta}$ for the five DNS runs from MU are shown in Table 1. These runs are identified as run1 through run5, with run1 corresponding to a base case ($\varepsilon = 0$), and the other four for turbulent cases at $\varepsilon = 95, 280, 656, 1535$ cm^2 s^{-3}, respectively. Table 1 also shows the number of colliding pairs detected and used to process the probability distributions, and the flow Taylor–microscale Reynolds number. The Reynolds numbers in DNS are about two orders of magnitude smaller than those in atmospheric clouds. Since the droplets are much smaller than the Kolmogorov eddy in air turbulence, and since terminal velocity is on the order of flow Kolmogorov velocity and the Stokes response time on the order of or less than the Kolmogorov time, the relative motion of cloud droplets is determined mainly by turbulent eddies in the viscous subrange. For this reason, the viscous dissipation rate is the key parameter in determining the droplet collision sta-

TABLE 2. The parameter setting, $\langle|\tilde{w}_r|\rangle$, and $\tilde{\sigma}_q$ for DNS runs conducted at UD ($a_1 = 30\ \mu$m, $a_2 = 20\ \mu$m, $\Delta W = 6.412$ cm s^{-1}).

Run ID	Run6	Run7	Run8	Run9	Run10	Run11
N	32	32	64	64	128	128
ε (cm^2 s^{-3})	100	400	100	400	100	400
dt (μs)	962.1	721.7	1110	555.1	898.2	449.1
$\tilde{\delta}$	1.235	0.926	1.425	0.712	1.153	0.576
No. of pairs	39 727	62 676	22 535	24 008	18 030	30 722
R_λ	23.4	23.4	43.0	43.0	72.4	72.4
$\tilde{w}_r$, DNS	1.016	1.123	1.038	1.128	1.032	1.122
$\tilde{\sigma}_q$, Eq. (30)	0.253	0.702	0.390	0.716	0.358	0.699

tistics. The flow Reynolds number is assumed to be of secondary importance here. Run2 through run5 were used in Franklin et al. (2005) to study effects of turbulence on geometric collision rate, and further details of the runs can be found there. The droplet radii were fixed to $a_1 = 20$ μm and $a_2 = 10$ μm, giving $\Delta W = 3.6958$ cm s^{-1}. Five distinct time step sizes were used in run1 through run5, leading to a range of $\tilde{\delta}$ from 0.0616 to 0.985. The values of $\langle|\tilde{w}_r|\rangle$ obtained from DNS are also listed in Table 1, followed by the values of $\tilde{\sigma}_q$ derived from Eq. (30). The magnitude of $\tilde{\sigma}_q$ will be a key input parameter for the theory to be developed next.

The six UD runs are listed in Table 2 and identified as run6 through run11. These represent two levels of ε and three levels of grid resolutions. The time steps are somewhat larger giving a value of $\tilde{\delta}$ from 0.576 to 1.425. The droplet size combination for these runs is $a_1 = 30$ μm and $a_2 = 20$ μm. The differential settling velocity ΔW is 6.412 cm s^{-1}. The numbers of collision pairs detected are roughly one order of magnitude larger than the MU runs. Again the key parameter $\tilde{\sigma}_q$ has been derived from Eq. (30) and listed in the table.

b. Formulation for a given q_r

We shall now examine the consequence of including q_r in the radial relative motion, in particular, its influence on the collision volume. For the moment q_r is assumed to be a constant and positive, and, therefore, will enhance the droplet–droplet radial relative motion toward each other. Within the concept of a collision sphere, a positive q_r enhances inward flux across the surface of the collision sphere. This then will expand the collision volume shown in Fig. 3 to one of the three geometric configurations shown in Fig. 5, depending on how $s \equiv q_r\, dt$ is compared to $\delta = \Delta W\, dt$. Because of the cylindrical symmetry of the collision volume, only the planar section through the axis of symmetry is shown in Fig. 5. For convenience, let us introduce $\tilde{s} \equiv s/R$.

The starting point is to realize that all a_1 droplets located in the spherical shell relative to a_2 droplets, $R \le r \le R + s$ would penetrate the collision-sphere surface within dt because of turbulent motion should there be no differential gravitational settling. Adding the differential gravitational settling is, to a first approximation, to shift the shell region upward by δ. The region formed during the shifting, but outside the original collision sphere, then constitutes the collision volume.

When $\tilde{s} < \sqrt{1 + \tilde{\delta}^2} - 1$ (case Ia), the shifted outer surface of the shell with radius equal to $(R + s)$ intercepts the original collision surface of radius R above the $\theta = \pi/2$ surface, that is, the line O–a–b in Fig. 5a. In this case, the effect of turbulence is to expand the collision volume from the base case volume formed by revolving

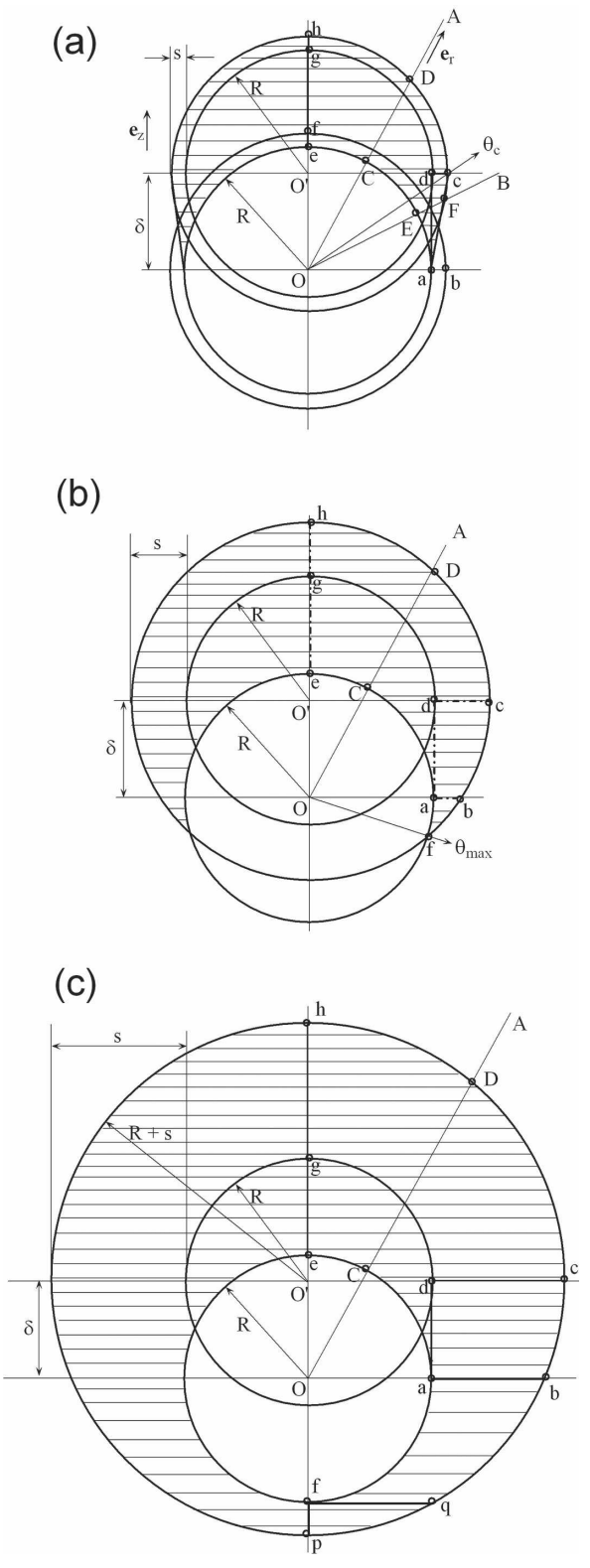

FIG. 5. The proposed regions that contribute to the geometric collisions when both gravity and air turbulence are considered and $q_r > 0$ (category I): (a) $s/R \le \sqrt{1 + \tilde{\delta}^2} - 1$; (b) $\sqrt{1 + \tilde{\delta}^2} - 1 < s/R \le \tilde{\delta}$; (c) $s/R > \tilde{\delta}$.

TABLE 3. Formula for V_{cv} and R_t in Eq. (32) for category I cases ($q_r > 0$).

Case Ia	$V_{cv}/(\pi R^3) = \tilde{\delta} + 2[(1+\tilde{s})^3 - 1]/3 + \tilde{\delta}\tilde{s}(1+\tilde{s}/3)$
$\tilde{s} < \sqrt{1+\tilde{\delta}^2} - 1$	$R_t/R = \tilde{\delta}\cos\theta + \sqrt{(1+\tilde{s})^2 - (\tilde{\delta}\sin\theta)^2}$, for $\theta < \theta_c$ $R_t/R = \tilde{\delta}/[\tilde{\delta}\sin\theta - \tilde{s}\cos\theta]$, for $\theta_c < \theta \le \pi/2$, where $\theta_c = \arctan[(1+\tilde{s})/\tilde{\delta}]$. Note $p(\theta; \tilde{\delta}, \tilde{s}) = 0$ for $\theta > \pi/2$.
Case Ib	$V_{cv}/(\pi R^3) = \tilde{\delta} + 2[(1+\tilde{s})^3 - 1]/3 + \tilde{\delta}(2\tilde{s} + \tilde{s}^2 - \tilde{\delta}^2/3) + (2\tilde{s} + \tilde{s}^2 - \tilde{\delta}^2)^2/(4\tilde{\delta})$
$\sqrt{1+\tilde{\delta}^2} - 1 \le \tilde{s} < \tilde{\delta}$	$R_t/R = \tilde{\delta}\cos\theta + \sqrt{(1+\tilde{s})^2 - (\delta\sin\theta)^2}$, for $\theta < \theta_{\max}$ where $\theta_{\max} = \arcsin[(2\tilde{s} + \tilde{s}^2 - \tilde{\delta}^2)/(2\tilde{\delta})] + \pi/2$. Note $p(\theta; \tilde{\delta}, \tilde{s}) = 0$ for $\theta > \theta_{\max}$
Case Ic	$V_{cv}/(\pi R^3) = \tilde{\delta} + 2[(1+\tilde{s})^3 - 1]/3 + \tilde{\delta}(2\tilde{s} + \tilde{s}^2 - \tilde{\delta}^2/3) + (2\tilde{s} + \tilde{s}^2 - \tilde{\delta}^2 - \tilde{\delta}] + (1+\tilde{s})^2(\tilde{s} - \tilde{\delta}) - [(1+\tilde{s})^3 - (1+\tilde{\delta})^3]/3$
$\tilde{s} \ge \tilde{\delta}$	$R_t/R = \tilde{\delta}\cos\theta + \sqrt{(1+\tilde{s})^2 - (\tilde{\delta}\sin\theta)^2}$.

the area a–d–g–f–e–C–E–a, to the shaded area shown in Fig. 5a. However, the maximum angle of approach remains 90°. There is a slight ambiguity in defining the portion a–c–d–a since in reality the gravity effect and turbulent motion occur simultaneously rather than in sequence as assumed here. As a simple yet reasonable choice we take a straight line connecting point c to point a as the boundary for that portion.

When $\sqrt{1+\tilde{\delta}^2} - 1 \le \tilde{s} < \tilde{\delta}$ (case Ib), the collision volume is shown as the shaded region in Fig. 5b and a portion of the collision volume has θ greater than 90°. This physically increases the range of the angle of approach as the intensity of turbulence motion is increased or $s/\delta = q_r/\Delta W$ is increased.

Finally, when $\tilde{s} \ge \tilde{\delta}$ (case Ic), the outer surface of the shifted shell completely covers the original collision sphere as shown in Fig. 5c. In this case, the larger droplets can approach the smaller droplets from any direction.

Having determined the collision volumes for $q_r > 0$, we now proceed to derive the probability distribution $p(\theta; \tilde{\delta}, \tilde{s})$ of angle of approach for a given $\tilde{\delta}$ and a given $\tilde{s}$. This probability can be computed as

$$p(\theta; \tilde{\delta}, \tilde{s})d\theta = \frac{2\pi \int_{r=R}^{r=R_t} r^2\, dr \sin\theta\, d\theta}{V_{cv}}, \qquad (31)$$

namely,

$$p(\theta; \tilde{\delta}, \tilde{s}) = \frac{2\pi \sin\theta (R_t^3 - R^3)}{3V_{cv}}, \qquad (32)$$

where V_{cv} denotes the total volume of the collision volume, $R_t(\theta)$ is the distance from the origin O of a point on the outer boundary of the collision volume with polar angle equal to θ. Both R_t and V_{cv} also depend on R, δ, and s. The formula for computing R_t and V_{cv} may be derived for all θ for each case. The details are somewhat laborious, and it is sufficient to present the final results in a readily usable form in Table 3. The correctness of the formula was checked by the following consistency condition

$$\int_{\theta=0}^{\theta=\pi} p(\theta; \tilde{\delta}, \tilde{s})\, d\theta = 1 \qquad (33)$$

for any $\tilde{\delta}$ or $\tilde{s}$. The angle θ_c and $\theta_{\max}$ in Table 3 for cases Ia and Ib are shown in Figs. 5a and 5b, respectively.

We shall next consider $q_r < 0$ in which the collision volume is reduced by outward relative motion caused by turbulence. It is necessary now to divide this into two categories. The first category (II) applies to $\delta < R$ and the cases under this category are depicted in Fig. 6. Let us define $s \equiv |q_r|dt$ and $\tilde{s} \equiv s/R$. In this category, the center of the shifted shell, which now has an inner radius $(R - s)$ and outer radius R, is located inside the original collision sphere. The collision volume is gradually reduced as s is increased. If $s > \delta$, then there is no collision volume outside the original collision sphere, and it is assumed $V_{cv} = 0$ and there is no need to obtain $p(\theta; \tilde{\delta}, \tilde{s})$. The difference between case IIa and case IIb is whether the interception point of the inner surface of the shifted shell with the horizontal plane passing through O′ is outside the original collision sphere or not. If the interception point is outside (case IIa), there are two transition angles θ_{c1} and θ_{c2}. The formula for V_{cv} and R_t for the cases in category II are provided in Table 4.

The category III is concerned with $q_r < 0$ and $R < \delta \le 2R$, and the cases are illustrated in Fig. 7. In category III, the center of the shifted shell is located outside the original collision sphere. A finite collision volume is permitted for all values of $s \equiv |q_r|dt$. In case IIIa, the inner surface of the shell overlaps with the original col-

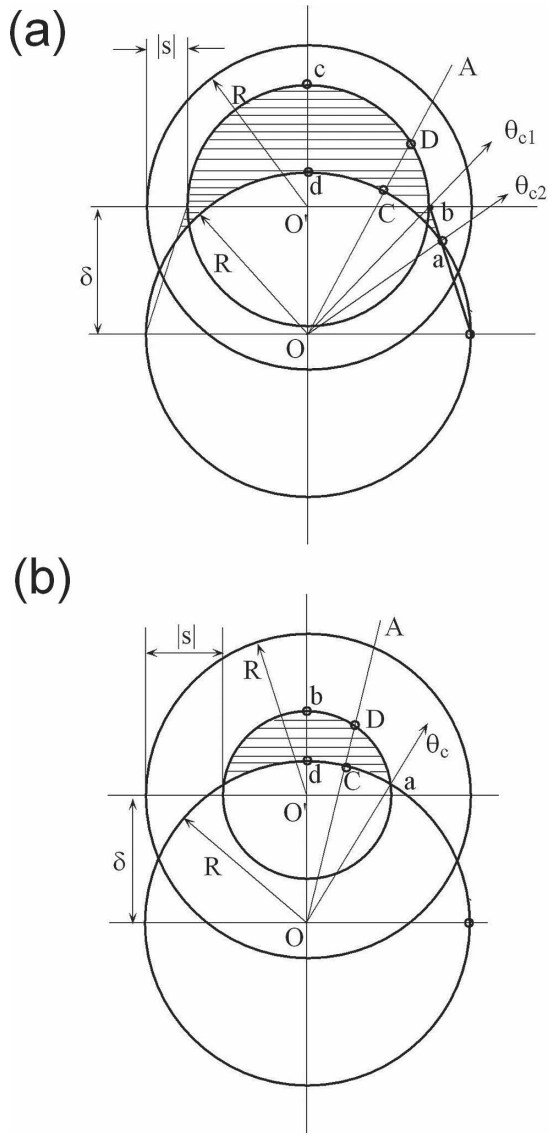

FIG. 6. The proposed regions that contribute to the geometric collisions when both gravity and air turbulence are considered, $q_r < 0$, and $\delta < R$ (category II): (a) $|s| \le R - \sqrt{R^2 - \delta^2}$; (b) $R - \sqrt{R^2 - \delta^2} < |s| \le \delta$. Note if $|s| > \delta$, the collision volume is zero.

lision sphere, while in case IIIb, the inner surface of the shell is completely outside the original collision sphere. When $s > R$ (case IIIc), the inner surface shrinks to a point, as shown in Fig. 7c. Again, there are ambiguities in defining certain portions of the outer boundary of the collision volume for category III cases. However, as will be shown later, the effect of turbulence will be mainly contributed by $q_r > 0$ because of a large relative weighting in the final integration, these ambiguities for $q_r < 0$ should have little impact on the final result. The formula for V_{cv} and R_t for the cases in category III are provided in Table 5.

All the category II and category III cases do not cause the maximum angle of approach to be larger than 90°. Therefore, only when $q_r\, dt > \sqrt{R^2 + \delta^2} - R$ (case Ib and case Ic) or when there is a sufficient radial inward motion due to turbulence, can the maximum angle of approach be made larger than 90°. There is no need to consider $\delta > 2R$, since all the DNS runs were performed with $\delta < 2R$.

As a summary of all the nine cases discussed above, the boundaries of all the cases are shown in Fig. 8 with the horizontal axis being $q_r\, dt/R$ and the vertical axis being $\tilde{\delta}$. For a given DNS run, $\tilde{\delta}$ is given, so $p(\theta; \tilde{\delta}, \tilde{s})$ can be obtained for all q_r from $-\infty$ to $+\infty$ using the relationship and formula discussed above. As q_r is increased from $-\infty$ to $+\infty$, the calculation of $p(\theta; \tilde{\delta}, \tilde{s})$ can involve going through cases IIc, IIb, IIa, Ia, Ib, and Ic in order for $\tilde{\delta} < 1$ or through cases IIIc, IIIb, IIIa, Ia, Ib, and Ic in order for $\tilde{\delta} > 1$.

c. Integration over q_r

The final step for obtaining probability distribution of θ is to integrate contributions from different levels of q_r. This is carried out by the following weighted integral

$$p(\theta; \tilde{\delta}, \tilde{\sigma}_q) = \int_{-\infty}^{\infty} \zeta(q_r) p(\theta; \tilde{\delta}, \tilde{s})\, dq_r, \tag{34}$$

where the weighting function is defined as

$$\zeta(q_r) = \frac{V_{cv}(q_r) p(q_r)}{\int_{-\infty}^{\infty} V_{cv}(q_r) p(q_r)\, dq_r}. \tag{35}$$

The weighting function is proportional to the flux or collision counts at a given q_r. Since the statistics realized by dynamic colliding pairs are of concern, such a weighting procedure is necessary. The weighting also ensures that the final distribution $p(\theta; \tilde{\delta}, \tilde{\sigma}_q)$ is properly defined such that

$$\int_{-\infty}^{\infty} p(\theta; \tilde{\delta}, \tilde{\sigma}_q)\, d\theta = 1. \tag{36}$$

This final distribution then depends on the two parameters $\tilde{\delta}$ and $\tilde{\sigma}_q$. The first parameter measures the effect of finite time interval dt as discussed in section 2. The second parameter measures the effect of air turbulence in modifying the probability distribution.

While it is difficult to perform the above integrations analytically, it is rather straightforward to integrate them numerically since all the components in the integral expressions are known analytically. The results to be presented in section 4 were based on numerical integrations using equal θ bins of width 1° and equal q_r

TABLE 4. Formula for V_{cv} and R_t in Eq. (32) for category II cases ($q_r < 0$ and $\tilde{\delta} \le 1$).

Case IIa	$V_{cv}/(\pi R^3) = (1-\tilde{s})^2(\tilde{\delta}-\tilde{s}) - [(1-\tilde{s})^3 - (1-\tilde{\delta})^3]/3 + (1-\tilde{\delta})[(1-\tilde{s})^2 - 1 + \tilde{\delta}] - \tilde{s}(\tilde{\delta}^2 - z_1^2)/\tilde{\delta} + (1+\tilde{s}^2/\tilde{\delta}^2)(\tilde{\delta}^3 - z_1^3)/3$
$\tilde{s} < 1 - \sqrt{1-\tilde{\delta}^2}$	$R_t/R = \tilde{\delta}\cos\theta + \sqrt{(1-\tilde{s})^2 - (\tilde{\delta}\sin\theta)^2}$, for $\theta < \theta_{c1}$ $R_t/R = \tilde{\delta}/[\tilde{\delta}\sin\theta + \tilde{s}\cos\theta]$, for $\theta_{c1} < \theta \le \theta_{c2}$, where $\theta_{c1} = \arctan[(1-\tilde{s})/\tilde{\delta}]$, $\theta_{c2} = 2\arctan(\tilde{\delta}/\tilde{s}) - \pi/2$, $z_1 = \tilde{\delta}/(\tilde{s} + \tilde{\delta}\tan\theta_{c2})$. Note $p(\theta; \tilde{\delta}, \tilde{s}) = 0$ for $\theta > \theta_{c2}$.
Case IIb	$V_{cv}/(\pi R^3) = (1-\tilde{s})^2(\tilde{\delta}-\tilde{s}) - [(1-\tilde{s})^3 - (1-\tilde{\delta})^3]/3 + (1-\tilde{\delta}-z_2)[(1-\tilde{s})^2 - 1 + \tilde{\delta}^2] + \tilde{\delta}[(1-\tilde{\delta})^2 - z_2^2]$
$1 - \sqrt{1-\tilde{\delta}^2} < \tilde{s} \le \tilde{\delta}$	$R_t/R = \tilde{\delta}\cos\theta + \sqrt{(1-\tilde{s})^2 - (\tilde{\delta}\sin\theta)^2}$, for $\theta < \theta_c$, where $\theta_c = \arccos(\tilde{\delta} + z_2)$, $z_2 = (2\tilde{s} - \tilde{\delta}^2 - \tilde{s}^2)/(2\tilde{\delta})$. Note $p(\theta; \tilde{\delta}, \tilde{s}) = 0$ for $\theta > \theta_c$.
Case IIc	$V_{cv} = 0$,
$\tilde{s} \ge \tilde{\delta}$	note $p(\theta; \tilde{\delta}, \tilde{s}) = 0$ for all θ.

bins of width $0.025\sigma_q$. It was also checked to ensure that the numerical results are unchanged when finer bins are used.

d. The probability distribution for $|w_{r,c}|$

The probability distribution $p(|w_{r,c}|; \tilde{\delta}, \tilde{\sigma}_q)$ of the radial relative velocity $|w_{r,c}|$ for colliding pairs is very different from that of the radial relative velocity $|w_r|$ for kinematic at-contact pairs. The method for obtaining $p(|w_{r,c}|; \tilde{\delta}, \tilde{\sigma}_q)$ is described next.

At the level of a given q_r, $|w_{r,c}|$ is directly related to θ as

$$|w_{r,c}| = |\Delta W \cos\theta + q_r|. \tag{37}$$

In terms of the dimensionless variable $|\tilde{w}_{r,c}|$, we have

$$|\tilde{w}_{r,c}| = \begin{cases} |2\cos\theta + 2\tilde{s}/\tilde{\delta}|, & \text{if} \quad q_r > 0; \\ |2\cos\theta - 2\tilde{s}/\tilde{\delta}|, & \text{if} \quad q_r < 0. \end{cases} \tag{38}$$

The conversion procedure starts with a given q_r or $\tilde{s}$, by mapping numerically the θ axis in $p(\theta; \tilde{\delta}, \tilde{s})$ to the $|\tilde{w}_{r,c}|$ axis in $p(|\tilde{w}_{r,c}|; \tilde{\delta}, \tilde{s})$, according to the above relationship between $|\tilde{w}_{r,c}|$ and θ, and that

$$p(\theta; \tilde{\delta}, \tilde{s})\, d\theta \to p(|\tilde{w}_{r,c}|; \tilde{\delta}, \tilde{s})\, d|\tilde{w}_{r,c}|. \tag{39}$$

Numerically, the θ axis was divided into 180 equal bins of width equal to 1°, and the $|\tilde{w}_{r,c}|$ axis was divided into 200 equal bins from $0 \le |\tilde{w}_{r,c}| \le 10\langle|\tilde{w}_r|\rangle$. The probability in each θ bin, $p(\theta; \tilde{\delta}, \tilde{s})\, d\theta$, is transferred to one, two, or more $|\tilde{w}_{r,c}|$ bins according to the θ to $|\tilde{w}_{r,c}|$ mapping. The amount received by a $|\tilde{w}_{r,c}|$ bin is equal to the θ bin probability times the percentage of the mapped $|\tilde{w}_{r,c}|$ range that falls into the $|\tilde{w}_{r,c}|$ bin. The probability for each $|\tilde{w}_{r,c}|$ bin is being accumulated as this procedure is applied to different θ bins in order. Finally, $p(|\tilde{w}_{r,c}|; \tilde{\delta}, \tilde{s})$ for a bin is equal to the accumulated probability divided by the $|\tilde{w}_{r,c}|$ bin width.

Next, $p(|\tilde{w}_{r,c}|; \tilde{\delta}, \tilde{\sigma}_q)$ is obtained by the same weighted integral

$$p(|\tilde{w}_{r,c}|; \tilde{\delta}, \tilde{\sigma}_q) = \int_{-\infty}^{\infty} \zeta(q_r) p(|\tilde{w}_{r,c}|; \tilde{\delta}, \tilde{s})\, dq_r. \tag{40}$$

This completes the calculation of $p(|\tilde{w}_{r,c}|; \tilde{\delta}, \tilde{\sigma}_q)$. Again, tests were done to ensure that the bin size has negligible effect on the final result.

4. Results and comparisons with DNS data

In this section, we compare the various theoretical expressions derived above with the 11 DNS runs introduced in section 3a and shown in Tables 1 and 2.

a. Theoretical predictions for the base case

First, in Fig. 9 we show the theoretical prediction for $p(\theta; \tilde{\delta})$ for the base case, given by Eq. (24), for four $\tilde{\delta}$ values corresponding to run2 through run5. The limiting case of $dt \to 0$ as given by Eq. (13) is also shown and it is symmetric with respect to $\theta = 45°$. For finite dt or $\tilde{\delta}$, the distribution is biased toward $\theta < 45°$ with the peak location moving to smaller θ with increasing $\tilde{\delta}$. When $\tilde{\delta} = 0.985$, the peak occurs at $\theta = 28°$.

The theoretical prediction is compared directly with DNS data for run1 ($\tilde{\delta} = 0.123$) in Fig. 10. Other than the numerical uncertainties in DNS data due to the limited number of collision pairs used, the data and the theory are in perfect agreement.

For the base case, run1, the statistical mean $\langle\theta\rangle$ and the standard deviation σ_θ for the angle of approach, calculated by discretizing the theoretical curves into bins of 1° width, are compared with DNS results in

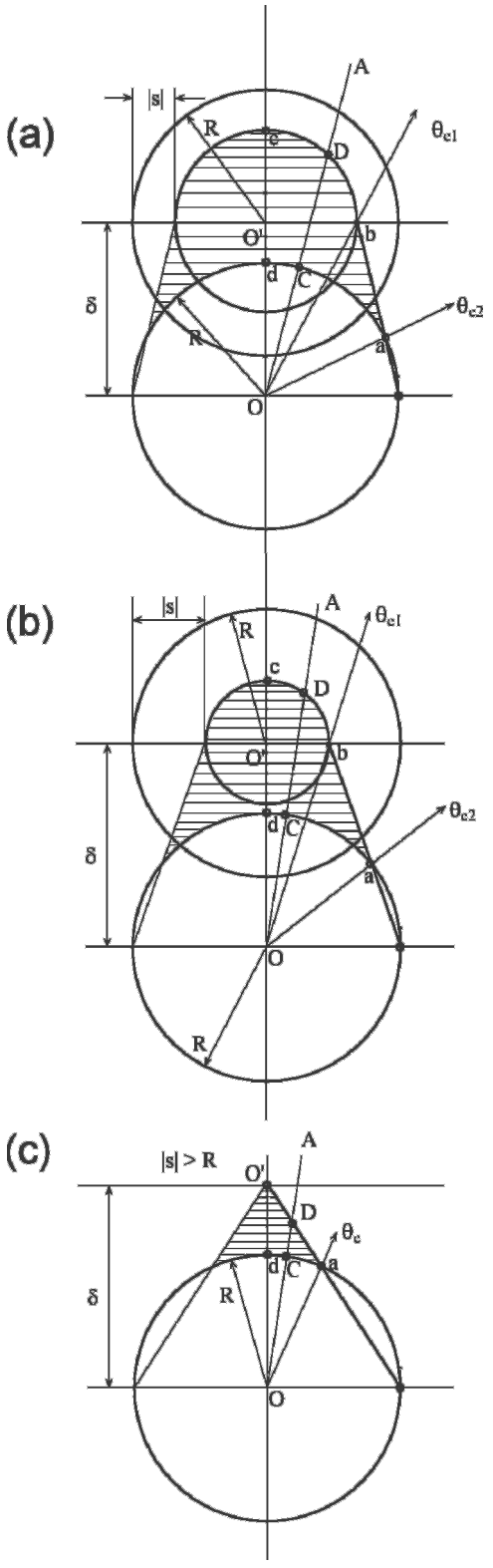

FIG. 7. The proposed regions that contribute to the geometric collisions when both gravity and air turbulence are considered, $q_r < 0$ and $R \le \delta < 2R$ (category III): (a) $|s| \le 2R - \delta$; (b) $2R - \delta < |s| \le R$; (c) $|s| > R$.

column 2 of Table 6. For this base case, the predicted mean value is essentially the same as the DNS result, and the predicted standard deviation agrees with the DNS value to within 1%.

Before the presentation of theoretical predictions for turbulent collision in the next subsection, we would like to point out that a significant portion of the changes in $\langle\theta\rangle$ for run2 through run5 is simply caused by the change in the time step size. To visually separate out the effect of air turbulence from the effect of time step size, we display in Fig. 11a the value of $\langle\theta\rangle$ for all 11 DNS runs (symbols) along with the theoretical value (the curve) for the base case, as a function of $\tilde{\delta}$. The open square represents run1 and lies exactly on the theoretical curve for the base case, and all other DNS data are located above the curve. The four stars, from right to left, denote the results of run2 through run5. The vertical distance of each data point above the curve may be viewed as representing the effect of turbulence after the effect of time step size being removed. Clearly, the effect of turbulence increases with ε. The three crossed circles represent the three UD runs at $\varepsilon = 100$ $\text{cm}^2\,\text{s}^{-3}$ and filled circles for the other three runs at $\varepsilon = 400$ $\text{cm}^2\,\text{s}^{-3}$. One may conclude, after removing the effect of time step, that the relative increase in $\langle\theta\rangle$ are about the same at a given level of ε. However, this effect of turbulence could also depend on other parameters such as the inertial response times of the droplets.

A similar plot (Fig. 11b) is constructed for the standard deviation σ_θ. Once again, part of the increase in σ_θ from run2 to run5 is caused by the decrease in dt. The change in σ_θ at a given ε is largely explained by the use of different dt.

The theory for $p(|\tilde{w}_{r,c}|; \tilde{\delta})$, given by Eq. (26), is compared directly with DNS data from run1 in Fig. 12. The data are well predicted by the theory clearly showing the parabolic dependence from very small $|\tilde{w}_{r,c}|$ and the related augmentation near $|\tilde{w}_{r,c}| = 2$ due to finite $\tilde{\delta}$. This shift can be intuitively explained by the reduced apparent angle of approach due to a finite time step, resulting in an increase in probability density for higher radial relative velocity. The predicted mean value for $|\tilde{w}_{r,c}|$ is essentially the same as the DNS result, and the predicted standard deviation agrees with the DNS value to within 7% (see Table 6).

An interesting observation from the data shown in Table 6 is the nonmonotonic behavior of $\langle|\tilde{w}_{r,c}|\rangle$ from run1 through run5 when ε is monotonically increased, as one would expect a monotonic increase due to the effect of turbulence. This can be explained by the effect of time step size. Unlike the case shown in Fig. 11 for $\langle\theta\rangle$, here the decreasing time step reduces $\langle|\tilde{w}_{r,c}|\rangle$ as shown clearly in Fig. 13. The monotonic increase can be

TABLE 5. Formula for V_{cv} and R_t in Eq. (32) for category III cases ($q_r < 0$ and $1 < \tilde{\delta} \le 2$).

Case IIIa $\tilde{s} \le 2 - \tilde{\delta}$	$V_{cv}/(\pi R^3) = 2(1 - \tilde{s})^3/3 + \tilde{\delta}[(1 - \tilde{s}/\tilde{\delta})^3 - (1 - \tilde{s})^3]/(3\tilde{s}) - \tilde{s}(1 - z_1^2)/\tilde{\delta} + (1 + \tilde{s}^2/\tilde{\delta}^2)(1 - z_1^3)/3$ $R_t/R = \tilde{\delta}\cos\theta + \sqrt{(1 - \tilde{s})^2 - (\tilde{\delta}\sin\theta)^2}$, for $\theta < \theta_{c1}$ $R_t/R = \tilde{\delta}/[\tilde{\delta}\sin\theta + \tilde{s}\cos\theta]$, for $\theta_{c1} < \theta \le \theta_{c2}$, where $\theta_{c1} = \arctan[(1 - \tilde{s})/\tilde{\delta}]$, $\theta_{c2} = 2\arctan(\tilde{\delta}/\tilde{s}) - \pi/2$, $z_1 = \tilde{\delta}/(\tilde{s} + \tilde{\delta}\tan\theta_{c2})$. Note $p(\theta; \tilde{\delta}, \tilde{s}) = 0$ for $\theta > \theta_{c2}$.
Case IIIb $2 - \tilde{\delta} < \tilde{s} < 1.0$	All the expressions are the same as in case IIIa
Case IIIc $\tilde{s} > 1$	$V_{cv}/(\pi R^3) = (\tilde{\delta} - 1)^3/(3\tilde{\delta}^2) + (1 + 1/\tilde{\delta}^2)(1 - z_1^3)/3 - (1 - z_1^2)/\tilde{\delta}$ $R_t/R = \tilde{\delta}/[\tilde{\delta}\sin\theta + \cos\theta]$, for $\theta < \theta_c$, where $\theta_c = 2\arctan(\tilde{\delta}) - \pi/2$, $z_1 = \tilde{\delta}/(1 + \tilde{\delta}\tan\theta_c)$ note $p(\theta; \tilde{\delta}, \tilde{s}) = 0$ for $\theta > \theta_c$.

restored if the vertical distance between the data and the base curve in Fig. 13a is used to measure the effect of turbulence. The competition between the effect of turbulence and the effect of time step size makes the statistics of $|\tilde{w}_{r,c}|$ particularly interesting. Overall, the effect of turbulence is similar for the mean and standard deviation of $|\tilde{w}_{r,c}|$, if the base case curve is taken as the reference. Another important observation is that the changes in the average relative velocity are mostly determined by the flow dissipation rate (Fig. 13a), while the changes in the mean angle of approach is mostly due to the time step size (see Fig. 11a).

b. Theoretical predictions for turbulent collisions

Let us first apply the theory for turbulent collision to run2 through run5. In Fig. 14, the weighting function ζ given by Eq. (35) is plotted as a function of $\tilde{q}_r$. Since the collision volume increases with $\tilde{q}_r$, the weighting function is biased toward positive $\tilde{q}_r$. In fact, the location where ζ obtains its maximum moves to larger $\tilde{q}_r$ as the level of air turbulence (i.e., the flow dissipation rate) is increased. Furthermore, the width of the ζ distribution also increases with the dissipation rate, implying that the probability distributions of θ and $|\tilde{w}_{r,c}|$ deviate more and more from their respective base case distribution.

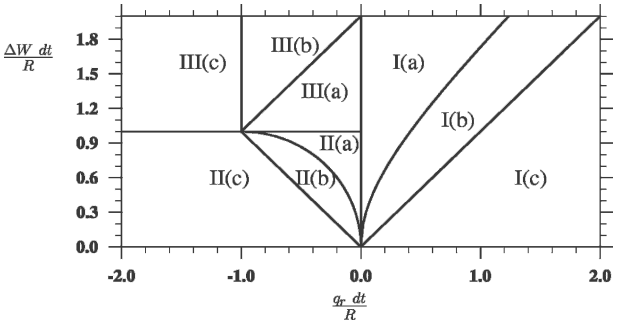

FIG. 8. The map for different regions as shown in Figs. 5–7.

The weighting functions for run6 through run11 can be obtained to yield similar results.

In Fig. 15, the probability distributions of the angle of approach for these runs are displayed. For each run, DNS data are shown as symbols, the base case theory is shown with a dashed line, and the theory for the turbulent case is denoted by a solid line. For the weak turbulence case (run2 in Fig. 15a), the present theory deviates only slightly from the base case curve, and both show a good agreement with the DNS data. The theory for the turbulent case is in excellent agreement with the DNS data for the other dissipation rate cases, as shown in Figs. 15b, 15c, and 15d. This shows that the theory captures the effect of turbulence well and the geometric interpretations are rather accurate. It is stressed that there is no adjustable parameter in the theory. We also note that if there is some numerical uncertainty in the value of $\langle|w_r|\rangle$ obtained from DNS, the performance of the theory will be affected as the

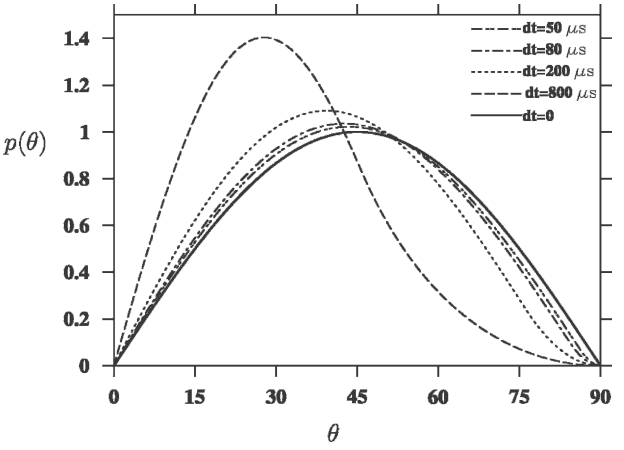

FIG. 9. The probability distribution of angle of approach for geometric gravitational collisions for four nonzero time step sizes used in Franklin et al. (2005) and for $dt \to 0$. Note that the probability density functions (PDFs) are defined with angle in radians (1 rad = 57.296°).

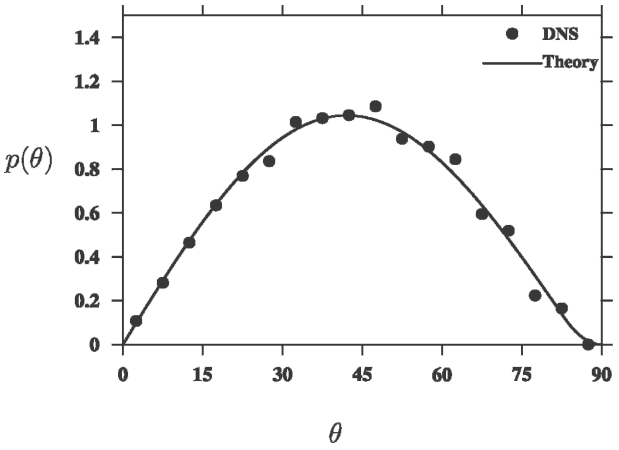

FIG. 10. The probability distribution of angle of approach for run1 compared with the theory. The DNS data were computed using a bin size of 5°.

input parameter σ_q may not be very accurate. No attempt is made to adjust the value of σ_q here. Similar conclusions can be drawn when the theory for $p(\theta)$ is compared to the data from run6 through run11 (plots not shown).

Let us now compare the mean and standard deviation of θ for colliding droplets obtained from the theory with the values obtained from DNS in Table 6. The relative difference between the theory and DNS for the mean is about 1% or less for run2 and run5. For run3 and run4, the relative difference is 2.2% and 2.4%, respectively. The standard deviation of θ was also well predicted, with slightly larger relative errors.

The statistics for θ are compared in Table 7 for run6 through run11. Both the mean and standard deviation are well predicted by the theory. The largest difference is seen for run9; and even for this case, the relative error of the theory is less than 6%.

Next, let us examine the probability distributions of $|\tilde{w}_{r,c}|$ for run2 and run5 in Fig. 16. Again, DNS data, base case theory, and the theory for the turbulent case are all shown for each case. Unlike $p(\theta)$ where the deviation from the base case is small for the weak turbulence case, DNS data show significant deviations even for run2. The present theory not only successfully predicts the shape of this deviation, but is quantitatively very accurate for all $|\tilde{w}_{r,c}|$. For the strong turbulence case, the probability distribution completely moves away from the base case curve. The present theory works well for $|\tilde{w}_{r,c}| < 1.5$ and gives a satisfactory curve

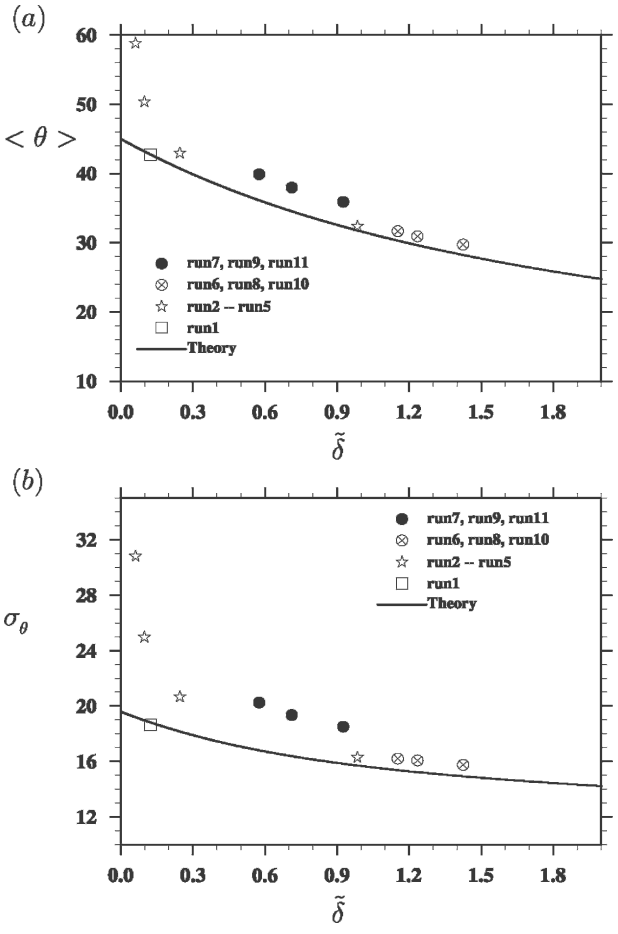

FIG. 11. Mean and standard deviation of θ as a function of $\tilde{\delta}$. The curve represents the theory for the base case.

TABLE 6. Comparison of the theory with DNS data for run1–run5.

ID	Run1	Run2	Run3	Run4	Run5
DNS, $\langle\theta\rangle$ (deg)	42.75 ± 0.37	32.41 ± 0.18	42.99 ± 0.36	50.40 ± 0.52	58.84 ± 0.59
DNS, σ_θ (deg)	18.67	16.31	20.68	24.99	30.83
Theory, $\langle\theta\rangle$ (deg)	42.76	32.05	43.92	49.21	58.90
Theory, σ_θ (deg)	18.82	15.84	20.88	23.98	30.49
DNS, $\langle\lvert\tilde{w}_{r,c}\rvert\rangle$	1.392 ± 0.009	1.692 ± 0.004	1.648 ± 0.011	1.935 ± 0.022	2.760 ± 0.037
DNS, $\sigma_{\lvert\tilde{w}_{r,c}\rvert}$	0.4334	0.3812	0.6272	1.069	1.915
Theory, $\langle\lvert\tilde{w}_{r,c}\rvert\rangle$	1.391	1.687	1.659	1.751	2.360
Theory, $\sigma_{\lvert\tilde{w}_{r,c}\rvert}$	0.3998	0.3534	0.6076	0.7612	1.159

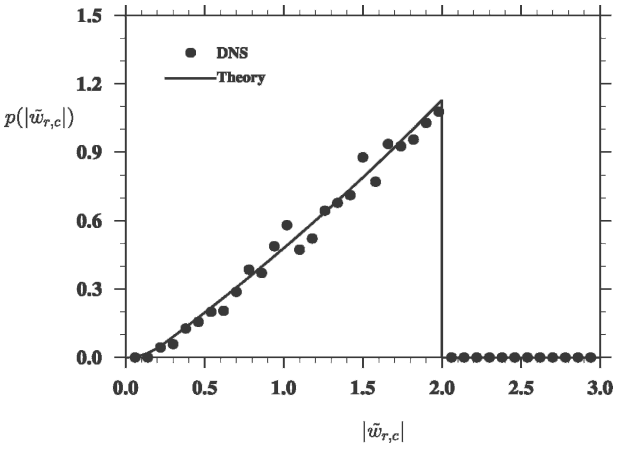

FIG. 12. The probability distribution of $|\tilde{w}_{r,c}|$ for run1 compared with the theory.

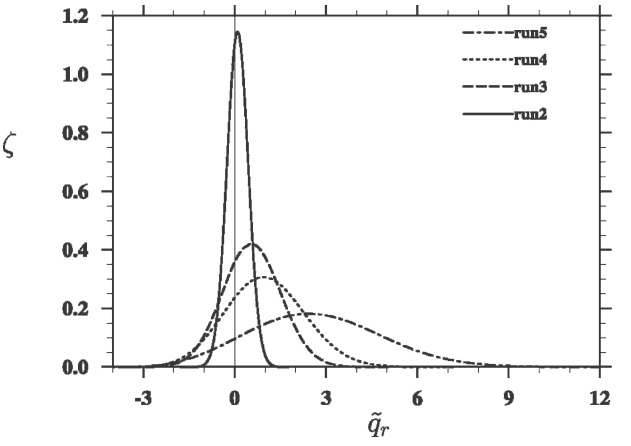

FIG. 14. The theoretical weighting function for run2–run5.

for $|\tilde{w}_{r,c}| > 1.5$. The DNS data show more intermittency for $|\tilde{w}_{r,c}| > 6$, perhaps due to non-Gaussian small-scale physics in DNS turbulence. The noticeable quantitative difference between the theory and the DNS data for this strong turbulence case indicates that the probability distributions of $|\tilde{w}_{r,c}|$ are more sensitive to the assumptions made in the theory such as the Gaussian probability distribution for q_r and sequential rather than simultaneous treatment of the gravity and turbulence effects.

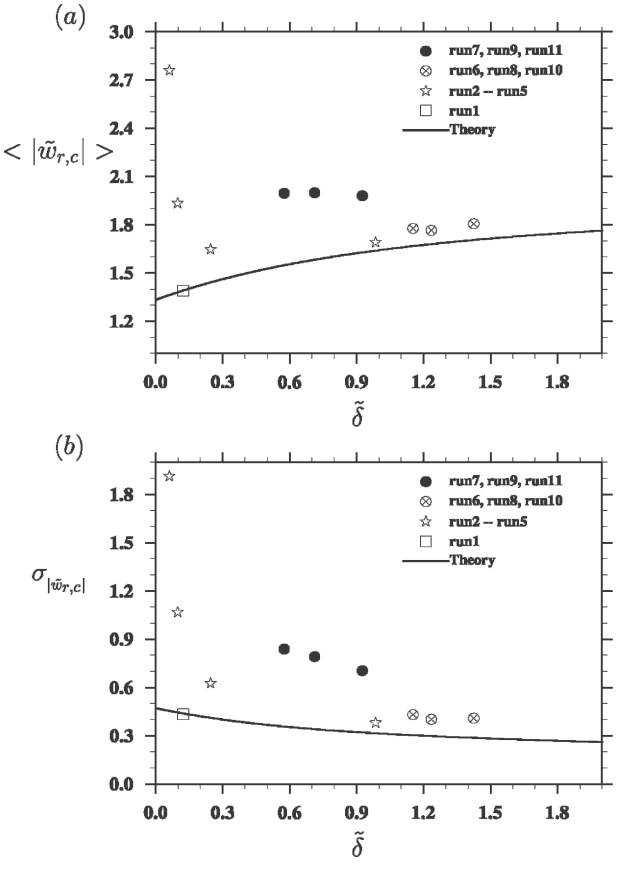

FIG. 13. Mean and standard deviation of $|\tilde{w}_{r,c}|$ as a function of $\tilde{\delta}$. The curve represents the theory for the base case.

The basic statistics for $|\tilde{w}_{r,c}|$ are compared in Table 6 for run2 through run5. The relative error in the predicted mean value of $|\tilde{w}_{r,c}|$ increases with the flow dissipation rate, and is 0.3%, 0.7%, 9.5%, and 14.5% for run2, run3, run4, and run5, respectively. The theory tends to underpredict $\langle|\tilde{w}_{r,c}|\rangle$ and the standard deviation $\sigma_{|\tilde{w}_{r,c}|}$ at higher levels of air turbulence. Both may be because of the inability of the theory to capture the high intermittency shown in DNS at large values of $|\tilde{w}_{r,c}|$. The theory can still be considered very satisfactory given that no parameter is adjusted and that the input parameter $\tilde{\sigma}_q$ may not be very accurate.

The average statistics of $|\tilde{w}_{r,c}|$ for run6 through run11 are listed in Table 7 for comparison. The maximum difference in $\langle|\tilde{w}_{r,c}|\rangle$ is less than 7% here, perhaps due to better estimations of $\langle|w_r|\rangle$ and, as such, of σ_q due to much larger numbers of pairs detected (see Tables 2 and 1 for information on the number of pairs detected). Larger dissipation rates for run4 and run5 may also contribute to the larger difference between the theoretical predictions and the DNS data.

Finally, a brief discussion of the relative motion associated with turbulent collisions of equal-sized droplets is presented. Although such self-collisions are not possible in stagnant air, they can occur when air turbulence is present. In Fig. 17, the probability distribution of angle of approach for $a_1 - a_1$ (i.e., 30 μm − 30 μm) self collisions in run11 is displayed, based on 7722 collision pairs numerically detected with dt = 449.1 μs.

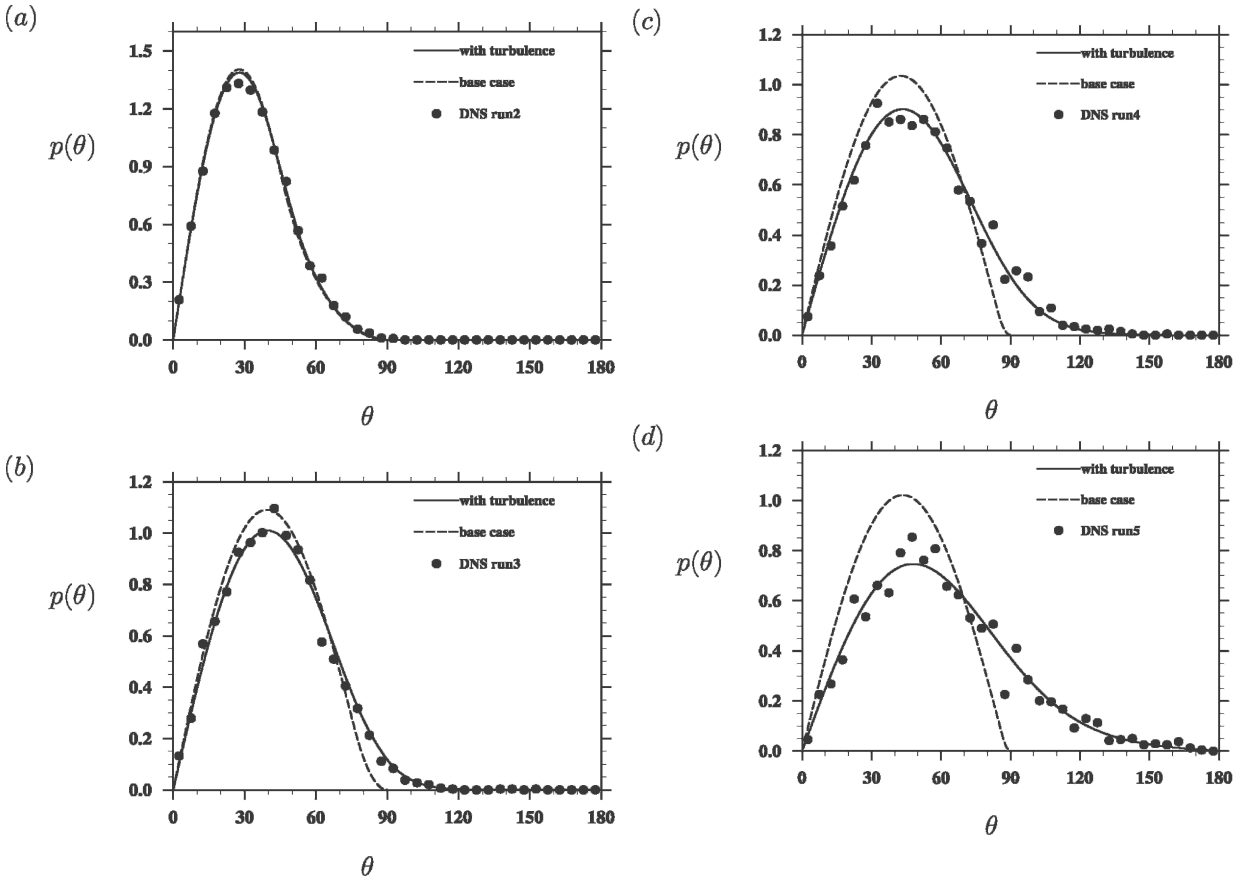

FIG. 15. The probability distributions of angle of approach from DNS are compared to the theory for the turbulent collision and the theory for the base case: (a) run2, (b) run3, (c) run4, and (d) run5.

Assuming the orientation for self-collision pairs is isotropic, the probability distribution would be given by Eq. (29). While this is roughly the case, the actual probability appears to be larger than the isotropic theory for $\theta < 50°$ and is smaller than the isotropic theory for $50° < \theta < 120°$. Note that average radial relative velocity $\langle|w_r|\rangle$ for 30 μm $-$ 30 μm kinematic at-contact pairs is only 0.0823 cm s^{-1} according to DNS, while the terminal velocity W_1 of 30-μm droplets is 11.542 cm s^{-1}, which is 140 times of $\langle|w_r|\rangle$. The Stokes number, the ratio of droplet inertial response time to the flow Kolmogorov time is 0.573 for this case. Therefore, even a very weak coupling of turbulent motion and the gravitational settling through the inertial effect of droplets will alter the isotropy of the angle of approach. Nevertheless, the isotropic theory predicts a mean and standard deviation for θ of 90° and 39.2° (i.e., $\sqrt{\pi^2/4 - 2}$ rad), respectively, still a very decent prediction as DNS gives a mean of 89.5° and a standard deviation of 42.2°.

The probability distribution for the radial relative ve-

TABLE 7. Comparison of the theory with DNS data for run6–run11.

ID	Run6	Run7	Run8	Run9	Run10	Run11
DNS, $\langle\theta\rangle$ (deg)	30.94	35.92	29.74	37.98	31.68	39.90
DNS, σ_θ (deg)	16.07	18.51	15.75	19.35	16.20	20.25
Theory, $\langle\theta\rangle$ (deg)	30.21	37.84	29.71	40.18	31.44	41.42
Theory, σ_θ (deg)	15.45	19.87	15.47	20.78	15.90	21.06
DNS, $\langle\lvert\tilde{w}_{r,c}\rvert\rangle$	1.765	1.981	1.806	1.999	1.777	1.996
DNS, $\sigma_{\lvert\tilde{w}_{r,c}\rvert}$	0.4021	0.7046	0.4095	0.7916	0.4316	0.8393
Theory, $\langle\lvert\tilde{w}_{r,c}\rvert\rangle$	1.768	2.113	1.913	2.041	1.832	1.961
Theory, $\sigma_{\lvert\tilde{w}_{r,c}\rvert}$	0.3659	0.6396	0.4365	0.6647	0.4236	0.6647

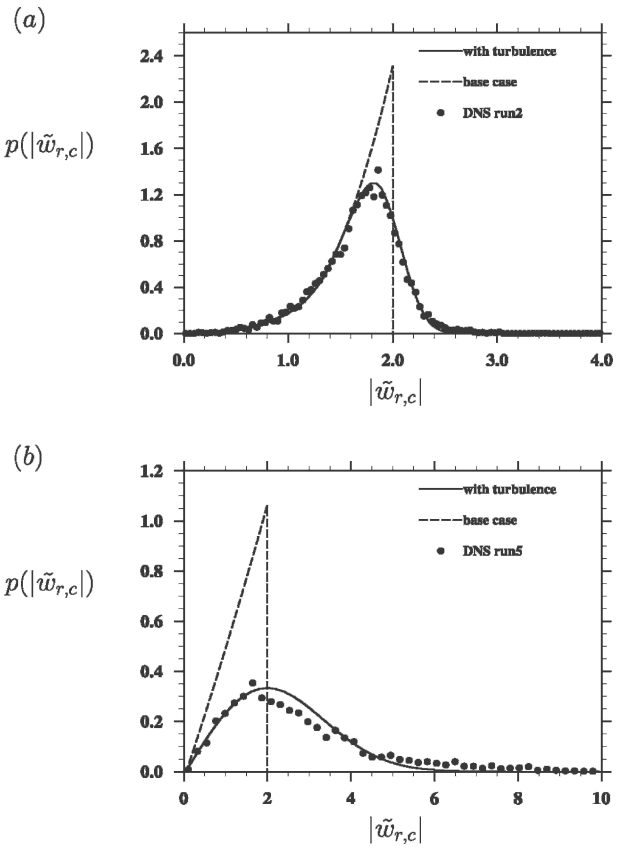

FIG. 16. The probability distributions of radial relative velocity for colliding droplets (a) run2 and (b) run5.

locity $|w_{r,c}|$ of dynamic colliding pairs is shown in Fig. 18. Also shown is a theory based on the Gaussian distribution, Eq. (28), weighted according to the local flux as

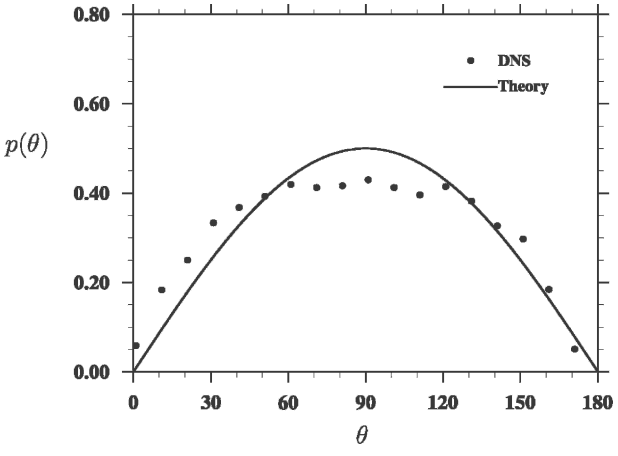

FIG. 17. The probability distribution of angle of approach for 30 μm–30 μm self-collisions run11.

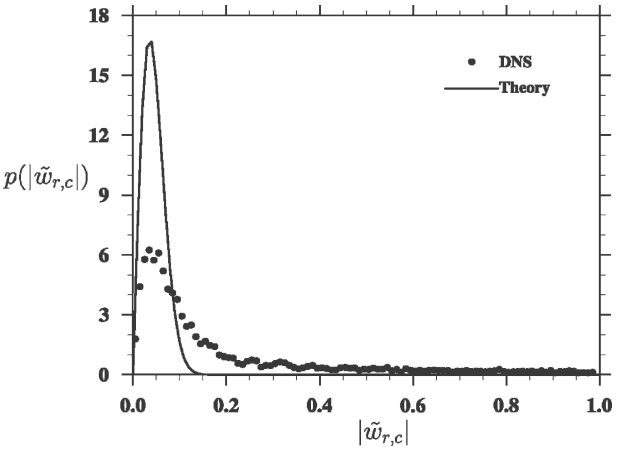

FIG. 18. The probability distribution of radial velocity for 30 μm–30 μm self-collisions in 128^3 DNS with $\varepsilon = 400$ cm^2 s^{-3}. The air turbulence is the same as in run11.

$$p(|w_{r,c}|) = \frac{|w_{r,c}|\, p(|q_r| = |w_{r,c}|)}{\int_0^\infty |w_{r,c}|\, p(|q_r| = |w_{r,c}|)\, d|w_{r,c}|} = \frac{|w_{r,c}|}{\sigma_q^2} \exp\left[-\frac{(|w_{r,c}|)^2}{2\sigma_q^2} \right] \tag{41}$$

with $\sigma_q = \langle |w_r| \rangle \sqrt{\pi/2}$. This simple theory, although giving a reasonable prediction of the peak location, is far from satisfactory for the reason indicated above, namely that a weak secondary coupling between the turbulent motion and settling due to finite droplet inertia may significantly broaden the distribution of relative velocity since $W_1 \gg \langle |w_r| \rangle$.

5. Summary

This study was motivated by the need to understand recent DNS results of the probability distribution of angle of approach θ and relative velocity $|\tilde{w}_{r,c}|$ for colliding droplet pairs in a turbulent flow (Franklin et al. 2005). First we developed a rigorous and thorough theory to predict all relevant probability distributions for gravitational collisions without air turbulence. In particular, it was shown that the probability distributions, calculated at the beginning of the time steps used for collision detection, can depend on the time step size. This effect of time step size can be quantified theoretically in terms of the nondimensional parameter $\tilde{\delta} = \Delta W dt/R$. The shape of these distributions is nontrivial when $\tilde{\delta}$ is not small. This finding is important in view of the facts that $\tilde{\delta}$ may not be small in the DNS simulations and that $\tilde{\delta}$ varies from one DNS run to another. Only by understanding this effect of time step size, can we cor-

rectly determine the true effect of air turbulence. We also illustrate that the statistical information for dynamic colliding pairs is very different from that of kinematic at contact pairs. This difference was previously noted for collisions because of a simple shear or nonuniform shears in isotropic turbulence (Mei and Hu 1999; Wang et al. 2000, 2005c).

The base case theory was shown to predict the DNS data well when the air turbulence is not present. We also demonstrate how one can effectively remove the effect of time step size for the turbulent collision case by using the base case theory as the reference.

For turbulent collisions, a novel theory has been developed to quantify the effect of turbulence on the statistics of the angle of approach and radial relative velocity for colliding pairs. When air turbulence is considered, the collision volume is increased with more contributions from larger inward relative motion caused by turbulent fluctuations. The theory employs a logical decomposition that facilitates the development of the extended collision volumes and the derivations of the probability distributions. The additive treatment of the radial relative motion worked well for the cases we considered, perhaps because the relative motion is largely governed by the gravity. At this stage, we cannot be certain how general this conclusion would be.

It is shown that the theory captures the essential physics of air turbulence and provides a quantitatively acceptable prediction of the statistics for the angle of approach. For example, the theory predicts $\langle\theta\rangle$ to within 5% for most numerical experiments. It is also shown that the probability distribution of relative velocity for collision pairs is more sensitive to the presence of air turbulence and also shows larger intermittency at large radial velocity. Even for the more difficult quantity $|\tilde{w}_{r,c}|$, the theory represents a significant improvement over the base case theory and is considered to be satisfactory as there is no adjustable parameter in the theory. Part of the success of the theory may be attributed to the use of the average kinematic relative velocity obtained directly from DNS. However, the derived probability distributions provide a thorough description of the angle of approach and the relative velocity for dynamically colliding pairs. It should be noted that the average kinematic relative velocity may be expressed theoretically in terms of droplet inertial response time, terminal velocity, flow dissipation rate, and Reynolds number (Saffman and Turner 1956; Kruis and Kusters 1997). Such a theoretical model can be incorporated into the current theory to eliminate the need of using any DNS result in the theory.

It is believed that the theoretical framework developed here could be of value to other problems involving gravitational settling and weak turbulence, such as parameterization of collision kernel and hydrodynamic interactions of droplets. The theoretical results will also be useful for proper interpretation of experimental results derived from observations at discrete times (Meng et al. 2004; Yang et al. 2005).

Acknowledgments. This study has been supported by the National Science Foundation through Grant ATM-0114100 and by the National Center for Atmospheric Research (NCAR). Part of the work was supported by the NCAR Faculty Fellowship program. LPW thanks Kay Sandoval of NCAR for her editorial comments. CNF thanks Dr. P. A. Vaillancourt of Meteorological Service of Canada and Professor M. K. Yau of McGill University for many helpful discussions.

REFERENCES

Arenberg, D., 1939: Turbulence as a major factor in the growth of cloud droplets. *Bull. Amer. Meteor. Soc.,* **20,** 444–445.

de Almeida, F. C., 1979: The collisional problem of cloud droplets moving in a turbulent environment. Part II: Turbulent collision efficiencies. *J. Atmos. Sci.,* **36,** 1564–1576.

Falkovich, G., A. Fouxon, and M. G. Stepanov, 2002: Acceleration of rain initiation by cloud turbulence. *Nature,* **419,** 151–154.

Franklin, C. N., P. A. Vaillancourt, M. K. Yau, and P. Bartello, 2005: Collision rates of cloud droplets in turbulent flow. *J. Atmos. Sci.,* **62,** 2451–2466.

Khain, A. P., and M. B. Pinsky, 1997: Turbulence effects on the collision kernel. II. Increase of the swept volume of colliding drops. *Quart. J. Roy. Meteor. Soc.,* **123,** 1543–1560.

Koziol, A. S., and H. G. Leighton, 1996: The effect of turbulence on the collision rates of small cloud drops. *J. Atmos. Sci.,* **53,** 1910–1920.

Kruis, F. E., and K. A. Kusters, 1997: The collision rate of particles in turbulent flow. *Chem. Eng. Comm.,* **158,** 201–230.

Manton, M. J., 1974: The effect of a simple shear flow upon the coalescence rate of water droplets. *Geophys. Fluid Dyn.,* **6,** 83–99.

Maxey, M. R., 1987: The gravitational settling of aerosol-particles in homogeneous turbulence and random flow fields. *J. Fluid Mech.,* **174,** 441–465.

Mei, R., and C. Hu, 1999: On the collision rate of small particles in turbulent flows. *J. Fluid Mech.,* **391,** 67–89.

Meng, H., G. Pan, Y. Pu, and S. H. Woodward, 2004: Holographic particle image velocimetry: From film to digital recording. *Meas. Sci. Tech.,* **15,** 673–685.

Pinsky, M. B., A. P. Khain, and M. Shapiro, 1999: Collision of small drops in a turbulent flow. Part I: Collision efficiency, problem formulation, and preliminary results. *J. Atmos. Sci.,* **56,** 2585–2600.

——, ——, and ——, 2000: Stochastic effects of cloud droplet hydrodynamic interaction in a turbulent flow. *Atmos. Res.,* **53,** 131–169.

Pruppacher, H. R., and J. D. Klett, 1997: *Microphysics of Clouds and Precipitation*. 2d ed. Kluwer Academic, 954 pp.

Reuter, G. W., R. de Villiers, and Y. Yavin, 1988: The collection kernel for two falling cloud drops subjected to random perturbations at a turbulent airflow: A stochastic model. *J. Atmos. Sci.,* **45,** 765–773.

Saffman, P. G., and J. S. Turner, 1956: On the collision of drops in turbulent clouds. *J. Fluid Mech.,* **1,** 16–30.

Seinfeld, J. H., and S. N. Pandis, 1997: *Atmospheric Chemistry and Physics: From Air Pollution to Climate Change.* John Wiley and Sons Inc., 1326 pp.

Smook, G. A., 1982: *Handbook for Pulp and Paper Technologists.* Canadian Pulp and Paper Association, 210 pp.

Sundaram, S., and L. R. Collins, 1997: Collision statistics in an isotropic, particle-laden turbulent suspension. *J. Fluid Mech.,* **335,** 75–109.

Tory, E. M., 1996: *Sedimentation of Small Particles in a Viscous Fluid.* Computational Mechanics Publications, 281 pp.

Wang, L.-P., A. S. Wexler, and Y. Zhou, 1998a: On the collision rate of small particles in isotropic turbulence. Part 1. Zero-inertia case. *Phys. Fluids,* **10,** 266–276.

——, ——, and ——, 1998b: Statistical mechanical descriptions of turbulent coagulation. *Phys. Fluids,* **10,** 2647–2651.

——, ——, and ——, 2000: Statistical mechanical descriptions of turbulent coagulation of inertial particles. *J. Fluid Mech.,* **415,** 117–153.

——, Y. Xue, O. Ayala, and W. W. Grabowski, 2005a: Effects of stochastic coalescence and air turbulence on the size distribution of cloud droplets. *J. Atmos. Res.*, in press.

——, O. Ayala, S. E. Kasprzak, and W. W. Grabowski, 2005b: Theoretical formulation of collision rate and collision efficiency of hydrodynamically interacting cloud droplets in turbulent atmosphere. *J. Atmos. Sci.,* **62***,* 3243–2450.

——, ——, and Y. Xue, 2005c: Reconciling the cylindrical formulation with the spherical formulation in the kinematic descriptions of collision kernel. *Phys. Fluids,* **17,** 067103, doi:10.1063/1.1928647.

Yang, W. D., A. B. Kostinski, and R. A. Shaw, 2005: Depth-of-focus reduction for digital in-line holography of particle fields. *Opt. Lett.,* **30,** 1303–1305.

Zhou, Y., A. S. Wexler, and L.-P. Wang, 2001: Modelling turbulent collision of bidisperse inertial particles. *J. Fluid Mech.,* **433,** 77–104.